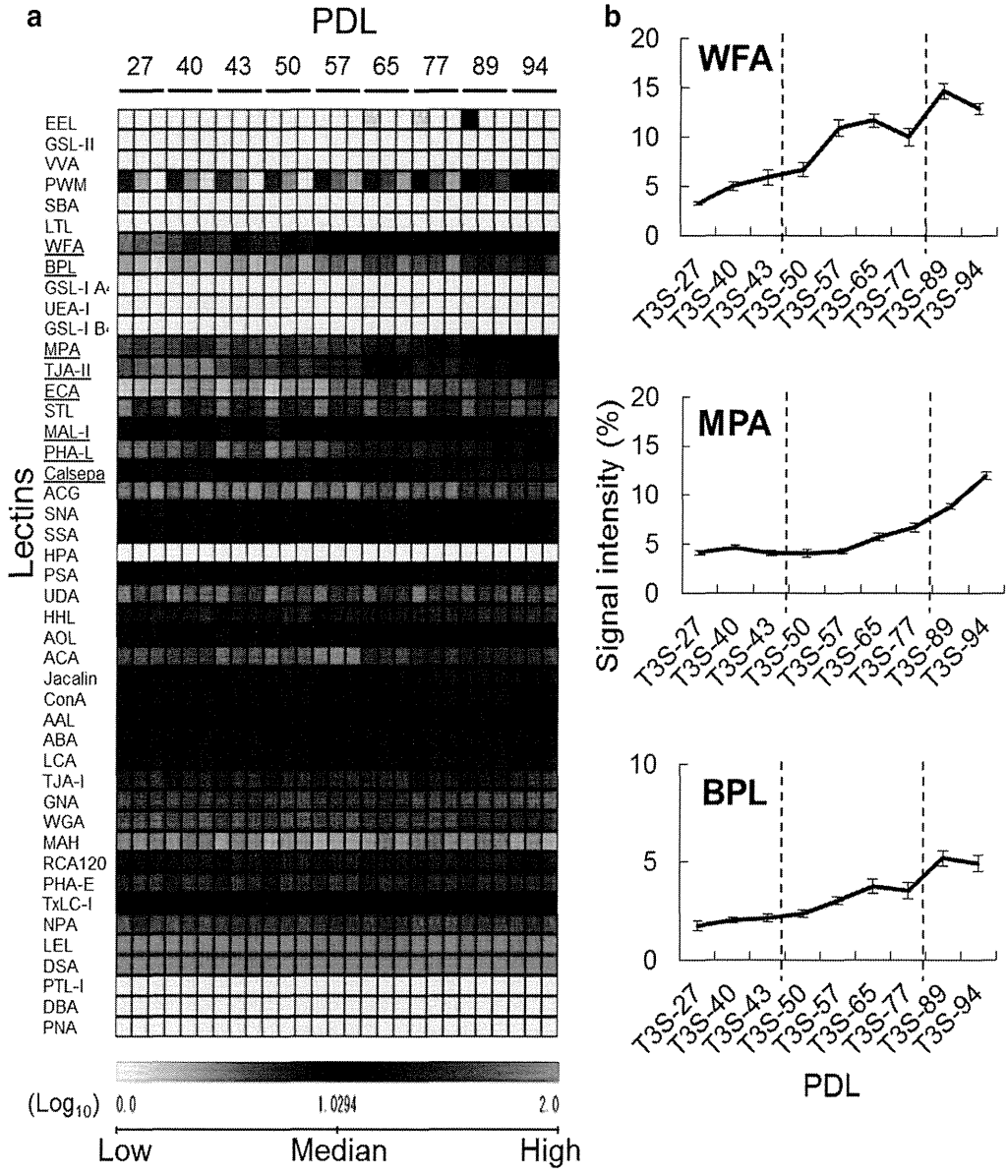

Fig. 2 Lectin microarray analysis of cellular senescence in TIG-3S fibroblasts at various PDLs. **a** Heat map representation of the (log_{10}-transformed) lectin microarray data from TIG-3S fibroblasts to compare the overall glycan profiles of the cells at different PDLs. The *rows* represent the lectins and the *columns* represent the PDLs (27–94). The *color scale* indicates low (*green*) to high (*red*) signal intensity. **b** *Line graph* representation of the signal intensity (%) at each PDL for changed lectins. There are three representative patterns including WFA, MPA and BPL. The data are represented as the mean ± SE (n = 3)

of passage-number, representing the gradual shift from young to aged cells. MAH plotted toward the positive direction and WFA plotted toward the negative direction of PC3. On the other hand, PC1 discriminated between TIG-3S and TIG-101/TIG-102, which plotted clearly toward the positive and the negative direction, respectively. ACG (Siaα2-3Galβ1-4GlcNAc-binder), SNA (Siaα2-6Gal-binders), and SSA (Siaα2-6Gal-binders) plotted toward the positive direction and PWM [$(GlcNAc)_n$- and $(Galβ1\text{-}4GlcNAc)_n$-binder] plotted toward the negative direction of PC1 as lectins differentiated these cells. Notably, aging TIG-3S PC1 localization approximated that of elderly-derived cells upon cellular senescence.

These results suggested that α2-3sialylation of the *O*-glycan form decreased with cellular senescence and α2-6sialylation of the *N*- and *O*-glycan forms and α2-3sialylation of the *N*-glycan form decreased with human aging.

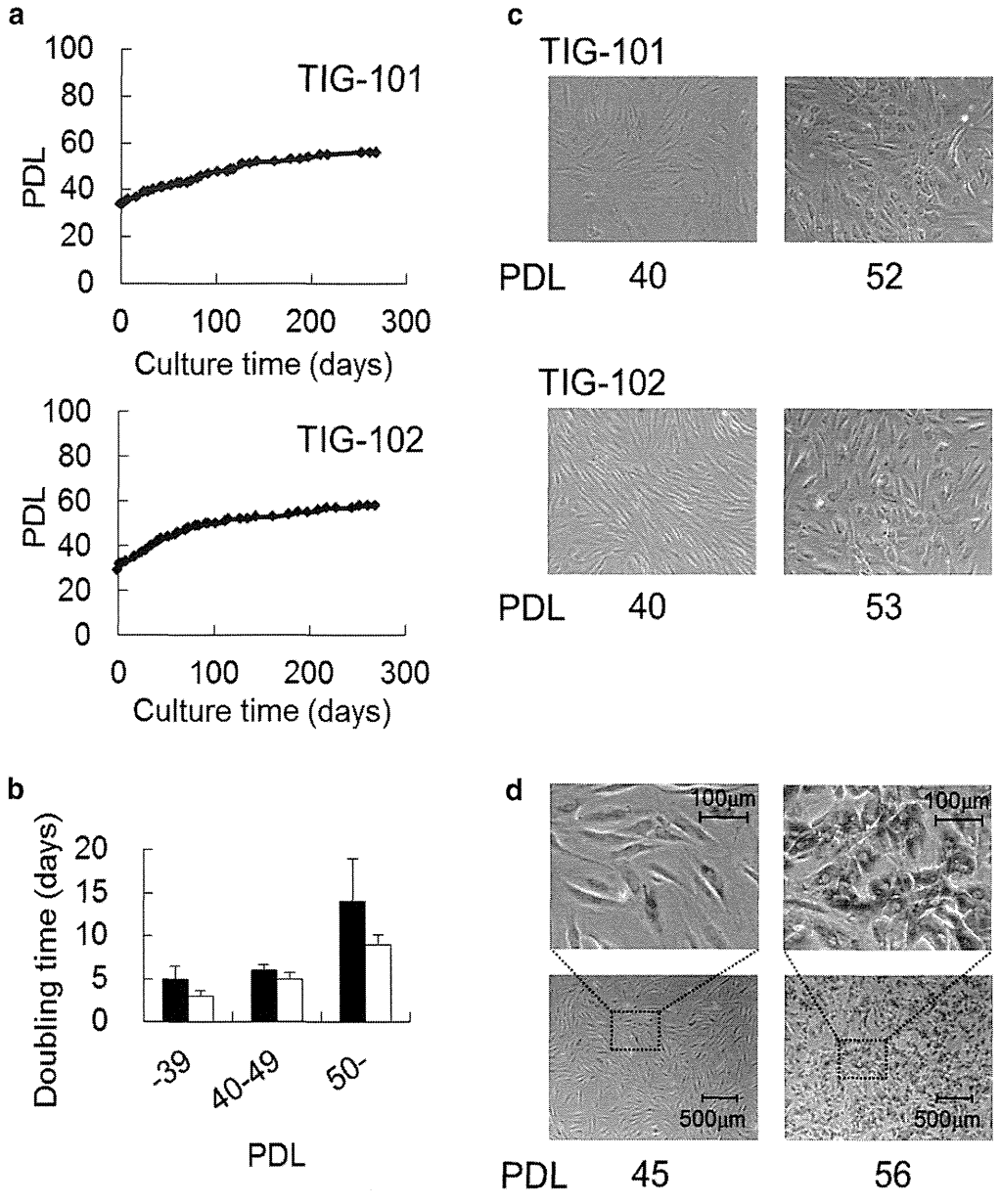

Fig. 3 Growth curves and morphologies of human diploid fibroblasts derived from elderly (TIG-101 and TIG-102). **a** TIG-101 and TIG-102 proliferation rates were plotted as PDL for approximately 280-day culture (each n = 1). **b** *Bar graph* representation of the average doubling time of the cells at each PDL (mean + SE, TIG-101: n = 4–10; TIG-102: n = 5–9). *Closed* and *opened bars* represent TIG-101 and TIG-102 cell lines, respectively. **c** Cell shapes of TIG-101 and TIG-102 fibroblasts at PDLs 40 and 52, and PDLs 40 and 53, respectively. **d** TIG-102 cells at PDLs 45 and 56 were stained for SA-β-galactosidase. The *upper panels* are a magnification of the squared area in the *lower panels*

Discussion

Late-passage cells exhibit various phenomena associated with cellular senescence such as elevated SA-β-galactosidase activity, cell hypertrophy, and decreased proliferative capacity in vitro. *In vivo*, signs of human aging such as a decline of biological function appear with chronological age. Thus, the accumulation of cellular senescence appears to influence human aging. The increase in various diseases with aging is likely induced by its negative effects on biological function. However, it is not clear whether a correlation exists between cellular senescence and human aging. To better understand human aging to facilitate treatment and prevention of its effects, we investigated the glycan profile changes associated with human cellular senescence and aging.

In this report, we compared glycan profile characteristics and continuous glycan changes between fetus- (TIG-3S) and elderly-derived (TIG-101 and TIG-102) cells. When the growth potential of TIG-3S cells declined after PDL 80, the glycan profile was found to be significantly

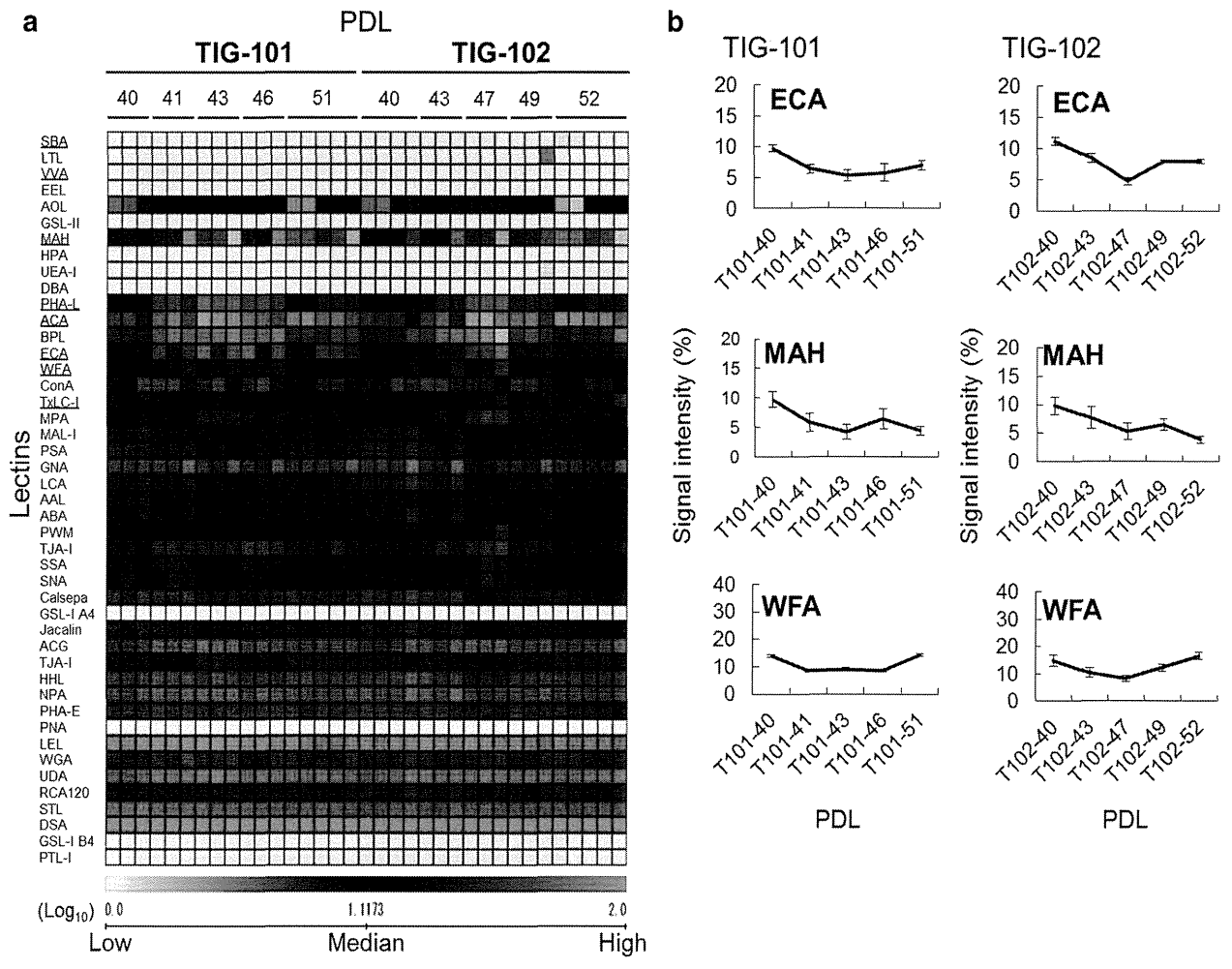

Fig. 4 Lectin microarray analysis of cellular senescence in TIG-101 and TIG-102 at various PDLs. **a** Heat map representation of the (log_{10}-transformed) lectin microarray data related to cellular senescence in the TIG-101 and TIG-102 cell lines. The *rows* represent lectins and the *columns* represent TIG-101 and TIG-102 cell lines at PDLs 40–51 and PDLs 40–52, respectively. The *color scale* indicates low (*green*) to high (*red*) signal intensity. **b** *Line graph* representation of the signal intensity (%) at each PDL for changed lectins. There are three representative patterns including ECA, MAH and WFA. The data are represented as the mean ± SE (n = 3–5)

changed. The glycan profiles of both elderly-derived lines were similarly changed at late passage. For example, the MPA signal in TIG-3S increased and TxLC-I in TIG-101 and TIG-102 decreased with passage. This suggests that the cellular senescence process was related to the change in glycan composition of the cell surface. As the WFA signal in TIG-3S significantly increased at middle passage (>PDL 50) prior to the morphological changes of cellular expansion and growth arrest, we reason that the glycan changes occurred before the morphological changes. Furthermore, the small alterations observed in the lectin microarray data from elderly-derived lines were consistent with their slow growth rate. Considering that the alteration of MAH and WFA signals significantly attributed to PC1, it appears that the Galβ1-3GalNAc structure was covered with α2-3Sia residues in early-passage cells and that the amount of α2-3sialilated *O*-glycans decreased with cellular senescence. Because of a deletion of the α2-3 Sia residues on *O*-glycans, the Galβ1-3GalNAc structures on *O*-glycans exposure increased with cellular senescence. Despite the relatively limited number of cell lines used in this study, these data were in agreement with those of independent analysis we performed in other fibroblasts and various other cell types (unpublished data).

On the other hand, the overall signals of the α2-6 and α2-3sialylated *N*-glycans and *O*-glycans of fetus-derived cells were significantly stronger than those of elderly-derived cells, although the profiles tended to converge upon late passages. At that time, the glycan profile of the fetus-derived cells had greatly changed and resembled that of elderly-derived cells. It has been previously

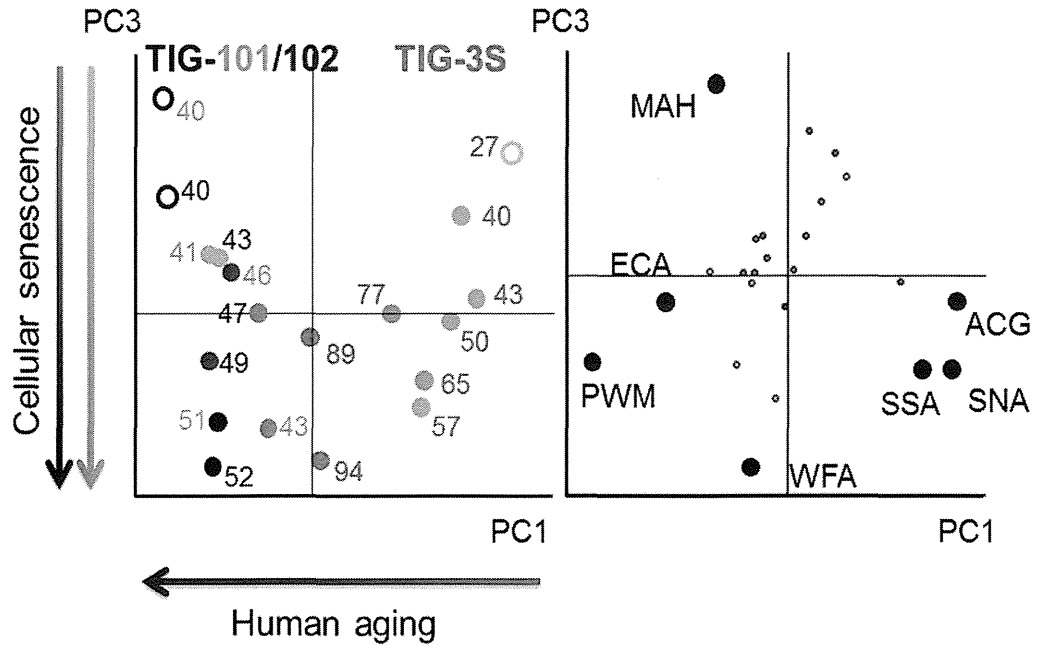

Fig. 5 Biplot for PCA analysis. PC1 represents human aging and PC3 represents cellular senescence. The *pink*, *light blue*, and *dark blue labels* represent TIG-3S, TIG-101, and TIG-102 cell lines, respectively. Color gradients (light to dark) reflect cellular senescence (young to aged). *Closed circles* represent distinguishable lectins of human aging or cellular senescence. *Left panel* cell passage replications; *right panel* lectin replications shown as a biplot

reported that fetal cell surface *N*-glycan α2-6 Sia residues decrease because of decreased ST6Gal I gene expression during cellular senescence [9]. Furthermore, extrinsic factor-induced rapid cellular senescence of adenocarcinoma cells leads to enhanced galactose residue cell surface exposure concomitant with increasing β1-4GalT [24]. Consequently, it has been suggested that desialylation impacts cellular senescence. Additionally, it has been shown that α2-3 and α2-6sialylation of *N*-glycans in adult tissue-derived cells of pregnant woman are altered during gestation and with age [25]. Functionally, the migration of human skin fibroblasts from elderly donors was found to be reduced and the migration was shown to differ between early- and late-passage cells by Kondo et al. in 1992 [24]. Thus, we speculate that the glycan changes of senescent cells are important for the mechanism of biological aging.

We note that the observed senescence-associated decreased sialylation and increased galactose exposure might be related to age-related disease as well as human aging. However, various sialylations have been often proposed as biomarkers for the genetic disease such as cancer [26]. This suggests that the mechanism of glycosylation differs between dysfunction with human aging, including age-related disease, and genetic disease. Therefore, we infer that desialylated senescent cells, which gradually accumulate in vivo, have detrimental effects on biological functions such as signal transduction and molecular recognition with human aging. To address these issues, quantitative analyses of detailed glycan changes associated with human aging and biological function will be required.

In addition to broadening our understanding of cellular function during aging in general, the establishment of a biomarker of cellular aging will facilitate the study of elderly patient-derived adult or stem cells, which are being used in various clinical trials [27–30]. It has been reported that stem cell aging is associated with the suppression of tissue regeneration and with malignant transformation [31, 32]. Disruption of these mechanisms possibly is an additional factor contributing to disease related to aging. Therefore, it is important to evaluate the potential efficacies of cells used as the source of regenerative therapy as well as to identify the optimal cells for such usage. Accordingly, knowledge of the glycan modifications present on aging cells will be useful in the identification of appropriate therapeutic cells.

Methods

Cell culture

The fetus-derived TIG-3S, 86-year-old subject-derived TIG-101, and 97-year-old subject-derived TIG-102 fibroblast cell lines were purchased from the Health Science Research Resources Bank (Osaka, Japan); the respective PDLs were 23, 34, and 29. Cell proliferative capacity was assessed by calculating the total number of PDLs using

Table 2 Population doubling levels (PDLs) applied for assessments

Cell line	PDL									
TIG-3S	27	40	43	50	57	65	77	83[b]	89	94
TIG-101	40	41	43	46	51	52[a]				
TIG-102	40	43	45[b]	47	49	52	53[a]	56[b]		

Cells were applied for morphological and histochemical analysis

[a] Only morphological observation

[b] Only histochemical stain

the formula PDL = $\log_2$(total number of cells/initial number of cells). Here, the PDL counts were rounded up after the decimal point. Cells were maintained in Dulbecco's modified Eagle medium (Wako Pure Chemical Industries, Osaka, Japan) containing 10 % fetal bovine serum (Cell Culture Technologies, Gravesano, Switzerland) supplemented with 50 U/ml penicillin and 50 μg/ml streptomycin (Gibco, Grand Island, NY, USA). All cultures were subcultivated in 100 mm plastic dishes (Falcon, San Jose, CA, USA) at 37 °C under humidified 5 % CO_2. When the cultures reached confluence at 3–4 days (TIG-3S) or 1–2 weeks (TIG-101 and TIG-102) of subcultivation, the cells were removed from the dish by treatment with 0.25 % trypsin–EDTA solution (IBL, Gunma, Japan) and subcultivated further using 0.4 to 0.5 × 10^6 cells. However, later passage cultures of TIG-101 and TIG-102 were subcultivated using 0.1 to 0.3 × 10^6 cells. The doubling time was calculated as the time in culture required for each PDL (days/PDL). All cell pellets were collected for assessment according to the PDLs shown in Table 2. For comparison of cell surface glycan profiles, cell pellets were subjected to lectin microarray analysis.

Senescence-associated β-galactosidase (SA-β-galactosidase) detection

SA-β-galactosidase activity in cultured cells was histochemically detected using the Senescence Detection Kit (Calbiochem, EMD Biosciences, Darmstadt, Germany). In brief, the culture medium was removed and the cultured cells were rinsed with 2 ml of phosphate-buffered saline (PBS) and then fixed with 1 ml of fixative solution at room temperature for 15 min. After rinsing with PBS, the cells were stained with 1 ml of staining solution mixture (staining solution: staining supplement: 20 mg/ml X-gal, 94:1:5) at 37 °C for 17 h. After incubation, the stained cells were observed under a microscope.

Lectin microarray analysis

Protein extracts of TIG-3S, TIG-101, and TIG-102 cell pellets (approximately 5 × 10^4 to 1 × 10^6 cells) collected at various PDLs were isolated as hydrophobic protein fractions using a CelLytic MEM Protein Extraction kit (Sigma, St. Louis, MO, USA) as described previously [23, 33]. Total proteins including glycoproteins (200 ng) were labeled with Cy3 mono-reactive dye (GE Healthcare, Buckinghamshire, UK) in PBS containing 0.5 % Triton X-100 at room temperature for 1 h. To remove excess Cy3 mono-reactive dye, the reaction solution was diluted with 20 μl of probing buffer (Tris-buffered saline containing 1 % Triton X-100, 1 mM $CaCl_2$, and 1 mM $MnCl_2$, pH 7.4), and applied to a spin-type desalting column loaded with Sephadex G-25 fine matrix (GE Healthcare). The Cy3-labeled glycoprotein solution (60 μl) was applied to a LecChip (Glyco Technica, Yokohama, Japan). After incubation at 4 °C for approximately 17 h, the reaction solution was discarded. The glass slide was washed three times with probing buffer before the LecChip was scanned using the evanescent-field fluorescence scanner GlycoStation™ Reader 1200 (Glyco Technica). Each sample was measured three to five times independently. All data were analyzed using GlycoStation™ Tools Signal Capture 1.0 and GlycoStation™ Tools Pro 1.0 (Glyco Technica). To expand the dynamic range, the data were subjected to a gain-merging procedure, and the merged data were normalized using max-normalization as described previously [19].

Statistical analysis

The lectin microarray data was analyzed using hierarchical clustering and PCA by means of pair-wise comparison, using http://www.lgsun.grc.nia.nih.gov/ANOVA/ (false discovery rate <0.05). The data was also analyzed and displayed using TIGR MultiExperiment Viewer (http://www.tm4.org/mev.html). The mean value of the lectin microarray data was used for each respective PCA.

Additional files

Additional file 1: Figure S1. Lectin microarray analysis of cellular senescence in TIG-3S fibroblasts at various PDLs. *Line graph* representation of signal intensity (%) at each PDL in selected significantly changed lectins. The signal intensities of MAL-I, Calsepa as well as MPA, changed at late passage. The signal intensities of TJA-II, ECA, PHA-L as well as BPL, changed during long passage. The data are represented as the mean ± SE (n = 3).

Heat map plots are shown in each *line graph* with the *color scale* indicating low (*blue*) to high (*yellow*) signal intensity.

Additional file 2: Figure S2. Lectin microarray analysis of cellular senescence in TIG-101 and TIG-102 fibroblasts at various PDLs. *Line graph* representation of signal intensity (%) at each PDL in selected changed lectins. The signal intensities of SBA, VVA, PHA-L as well as ECA, first decreased and then slightly increased. The signal intensities of TxLC-I, ACA as well as MAH, decreased gradually. The data are represented as the mean ± SE (n = 3–5). Heat map plots are shown in each *line graph* with the *color scale* indicating low (*blue*) to high (*yellow*) signal intensity.

Additional file 3: Figure S3. Lectin microarray analysis of TIG-3S, TIG-101, and TIG-102 cell lines at various PDLs. Heat map representation of the (log_{10}-transformed) lectin microarray data. The *rows* represent the lectins and the *columns* represent TIG-3S, TIG-101, and TIG-102 cell lines at PDLs 27–94, PDLs 40–51 and PDLs 40–52, respectively. The *color scale* indicates low (*green*) to high (*red*) signal intensity.

Additional file 4: Figure S4. Hierarchical clustering of glycan profile for TIG-3S (*pink*), TIG-101 (*light blue*), and TIG-102 (*dark blue*). The lectin microarray data were analyzed at PDLs 27–94, PDLs 40–51, and PDLs 40–52, respectively.

Abbreviations

Fuc: fucose; Gal: galactose; GalNAc: *N*-acetylgalactosamine; Glc: glucose; GlcNAc: *N*-acetylglucosamine; Man: mannose; PBS: phosphate-buffered saline; PCA: principal component analysis; PDL: population doubling level; SA-β-galactosidase: senescence-associated β-galactosidase; Sia: sialic acid.

Authors' contributions

YI designed the overall study, performed most of experiment, analyzed data and prepared the manuscript. NS contributed to manuscript writing. DK helped in the experiments of cell-culture. MT also conceived the idea and edited the manuscript. SG and AU provided suggestions for the study. All authors read and approved the final manuscript.

Author details

[1] Research Team for Geriatric Medicine (Vascular Medicine), Tokyo Metropolitan Institute of Gerontology, 35-2 Sakae-cho, Itabashi-ku, Tokyo 173-0015, Japan. [2] Department of Regenerative Medicine, Kyoto Prefectural University of Medicine, 465 Kajii-cho, Kawaramachi-Hirokoji, Kamigyo-ku, Kyoto 602-8566, Japan. [3] Department of Reproductive Biology, National Research Institute for Child Health and Development, 2-10-1 Okura, Setagaya-ku, Tokyo 157-8535, Japan.

Acknowledgements

This research was supported by the Kato Memorial Bioscience Foundation, by grants from the Ministry of Education, Culture, Sports, Science and Technology (MEXT) of Japan (No. 22890249, 24790397, and 25670182), by grants from the Ministry of Health Labor and Welfare (H25-saisei-shitei-013), and by The NOVARTIS Foundation (Japan) for the Promotion of Science.

Competing interests

The authors declare that they have no competing interests.

Received: 21 November 2015 Accepted: 3 February 2016
Published online: 18 February 2016

References

1. Ruhaak LR, Koeleman CA, Uh HW, Stam JC, van Heemst D, Maier AB, et al. Targeted biomarker discovery by high throughput glycosylation profiling of human plasma alpha1-antitrypsin and immunoglobulin A. PLoS One. 2013;8(9):e73082.
2. Kristic J, Vuckovic F, Menni C, Klaric L, Keser T, Beceheli I, et al. Glycans are a novel biomarker of chronological and biological ages. J Gerontol A Biol Sci Med Sci. 2014;69(7):779–89.
3. Ding N, Nie H, Sun X, Sun W, Qu Y, Liu X, et al. Human serum N-glycan profiles are age and sex dependent. Age Ageing. 2011;40(5):568–75.
4. Ohashi M, Aizawa S, Ooka H, Ohsawa T, Kaji K, Kondo H, et al. A new human diploid cell strain, TIG-1, for the research on cellular aging. Exp Gerontol. 1980;15(2):121–33.
5. Matuoka K, Mitsui Y. Changes in cell-surface glycosaminoglycans in human diploid fibroblasts during in vitro aging. Mech Ageing Dev. 1981;15(2):153–63.
6. Yamamoto K, Yamamoto M. Changes in the cell surface of human diploid fibroblasts during cellular aging. Mutat Res. 1991;256(2–6):169–75.
7. Toda T, Kaji K, Kimura N. TMIG-2DPAGE: a new concept of two-dimensional gel protein database for research on aging. Electrophoresis. 1998;19(2):344–8.
8. Takubo K, Aida J, Izumiyama N, Ishikawa N, Fujiwara M, Poon SS, et al. Chromosomal instability and telomere lengths of each chromosomal arm measured by Q-FISH in human fibroblast strains prior to replicative senescence. Mech Ageing Dev. 2010;131(10):614–24.
9. Tadokoro T, Yamamoto K, Kuwahara I, Fujisawa H, Ikekita M, Taniguchi A, et al. Preferential reduction of the alpha-2-6-sialylation from cell surface N-glycans of human diploid fibroblastic cells by in vitro aging. Glycoconj J. 2006;23(5–6):443–52.
10. Spataro AC, Bosmann HB, Myers-Robfogel MW. Sialyltransferase activities of aging diploid fibroblasts. Biochim Biophys Acta. 1979;553(3):378–87.
11. Blondal JA, Dick JE, Wright JA. Membrane glycoprotein changes during the senescence of normal human diploid fibroblasts in culture. Mech Ageing Dev. 1985;30(3):273–83.
12. Mann PL, Swartz CM, Holmes DT. Cell surface oligosaccharide modulation during differentiation: III. Lectin affinity class distributions. Mech Ageing Dev. 1988;44(1):1–16.
13. Mann PL, Lopez-Colberg I, Kelley RO. Cell surface oligosaccharide modulation during differentiation. I. Modulation of lectin binding. Mech Ageing Dev. 1987;38(3):207–17.
14. Kuno A, Uchiyama N, Koseki-Kuno S, Ebe Y, Takashima S, Yamada M, et al. Evanescent-field fluorescence-assisted lectin microarray: a new strategy for glycan profiling. Nat Methods. 2005;2(11):851–6.
15. Pilobello KT, Slawek DE, Mahal LK. A ratiometric lectin microarray approach to analysis of the dynamic mammalian glycome. Proc Natl Acad Sci USA. 2007;104(28):11534–9.
16. Tateno H, Uchiyama N, Kuno A, Togayachi A, Sato T, Narimatsu H, et al. A novel strategy for mammalian cell surface glycome profiling using lectin microarray. Glycobiology. 2007;17(10):1138–46.
17. Uchiyama N, Kuno A, Tateno H, Kubo Y, Mizuno M, Noguchi M, et al. Optimization of evanescent-field fluorescence-assisted lectin microarray for high-sensitivity detection of monovalent oligosaccharides and glycoproteins. Proteomics. 2008;8(15):3042–50.
18. Hirabayashi J, Kuno A, Tateno H. Lectin-based structural glycomics: a practical approach to complex glycans. Electrophoresis. 2011;32(10):1118–28.
19. Kuno A, Itakura Y, Toyoda M, Takahashi Y, Yamada M, Umezawa A, et al. Development of a data-mining system for differential profiling of cell glycoproteins based on lectin microarray. J Proteomics Bioinform. 2008;1(2):68–72.
20. Tao SC, Li Y, Zhou J, Qian J, Schnaar RL, Zhang Y, et al. Lectin microarrays identify cell-specific and functionally significant cell surface glycan markers. Glycobiology. 2008;18(10):761–9.
21. Toyoda M, Yamazaki-Inoue M, Itakura Y, Kuno A, Ogawa T, Yamada M, et al. Lectin microarray analysis of pluripotent and multipotent stem cells. Genes Cells. 2011;16(1):1–11.
22. Tateno H, Toyota M, Saito S, Onuma Y, Ito Y, Hiemori K, et al. Glycome diagnosis of human induced pluripotent stem cells using lectin microarray. J Biol Chem. 2011;286(23):20345–53.
23. Itakura Y, Kuno A, Toyoda M, Umezawa A, Hirabayashi J. Podocalyxin-targeting comparative glycan profiling reveals difference between human embryonic stem cells and embryonal carcinoma cells. J Glycomics Lipidomics. 2013;S5:004.
24. Kondo H, Yonezawa Y. Changes in the migratory ability of human lung and skin fibroblasts during in vitro aging and in vivo cellular senescence. Mech Ageing Dev. 1992;63(3):223–33.
25. Robajac D, Masnikosa R, Vanhooren V, Libert C, Mikovic Z, Nedic O. The *N*-glycan profile of placental membrane glycoproteins alters during gestation and aging. Mech Ageing Dev. 2014;138:1–9.
26. Nakagoe T, Fukushima K, Nanashima A, Sawai T, Tsuji T, Jibiki M, et al. Expression of Lewis(a), sialyl Lewis(a), Lewis(x) and sialyl Lewis(x) antigens

as prognostic factors in patients with colorectal cancer. Can J Gastroenterol. 2000;14(9):753–60.
27. Cheng Z, Ito S, Nishio N, Xiao H, Zhang R, Suzuki H, et al. Establishment of induced pluripotent stem cells from aged mice using bone marrow-derived myeloid cells. J Mol Cell Biol. 2011;3(2):91–8.
28. Suzuki H, Shibata R, Kito T, Yamamoto T, Ishii M, Nishio N, et al. Comparative angiogenic activities of induced pluripotent stem cells derived from young and old mice. PLoS One. 2012;7(6):e39562.
29. Kondo T, Asai M, Tsukita K, Kutoku Y, Ohsawa Y, Sunada Y, et al. Modeling Alzheimer's disease with iPSCs reveals stress phenotypes associated with intracellular Abeta and differential drug responsiveness. Cell Stem Cell. 2013;12(4):487–96.
30. Yoshida T, Ozawa Y, Suzuki K, Yuki K, Ohyama M, Akamatsu W, et al. The use of induced pluripotent stem cells to reveal pathogenic gene mutations and explore treatments for retinitis pigmentosa. Mol Brain. 2014;7:45.
31. Zanussi S, Serraino D, Dolcetti R, Berretta M, De Paoli P. Cancer, aging and immune reconstitution. Anticancer Agents Med Chem. 2013;13(9):1310–24.
32. Kikushige Y, Miyamoto T. Hematopoietic stem cell aging and chronic lymphocytic leukemia pathogenesis. Int J Hematol. 2014;100:335–40.
33. Itakura Y, Kimura M, Gojo S, Toyoda M, Kami D, Motomura N, et al. Glycan profiling using a lectin microarray is a novel validation tool for monitoring the damage to freeze-thawed cells. Low Temp Med. 2011;37(3):71–7.

Genomics Data 6 (2015) 4–6

Contents lists available at ScienceDirect

Genomics Data

journal homepage: http://www.journals.elsevier.com/genomics-data/

Data in Brief

Whole-exome sequencing of fibroblast and its iPS cell lines derived from a patient diagnosed with xeroderma pigmentosum

Kohji Okamura [a], Masashi Toyoda [b], Kenichiro Hata [c], Kazuhiko Nakabayashi [c], Akihiro Umezawa [d,*]

[a] Department of Systems BioMedicine, National Research Institute for Child Health and Development, Tokyo 157-8535, Japan
[b] Department of Research Team for Geriatric Medicine, Tokyo Metropolitan Institute of Gerontology, Tokyo 173-0015, Japan
[c] Department of Maternal–Fetal Biology, National Research Institute for Child Health and Development, Tokyo 157-8535, Japan
[d] Department of Reproductive Biology, National Research Institute for Child Health and Development, Tokyo 157-8535, Japan

ARTICLE INFO

Article history:
Received 9 July 2015
Accepted 12 July 2015
Available online 20 July 2015

Keywords:
Xeroderma pigmentosum
Patient iPS cell
Sun burn
Suntan
Melanoma

ABSTRACT

Cells from a patient with a DNA repair-deficiency disorder are anticipated to bear a large number of somatic mutations. Because such mutations occur independently in each cell, there is a high degree of mosaicism in patients' tissues. While major mutations that have been expanded in many cognate cells are readily detected by sequencing, minor ones are overlaid with a large depth of non-mutated alleles and are not detected. However, cell cloning enables us to observe such cryptic mutations as well as major mutations. In the present study, we focused on a fibroblastic cell line that is derived from a patient diagnosed with xeroderma pigmentosum (XP), which is an autosomal recessive disorder caused by a deficiency in nucleotide excision repair. By making a list of somatic mutations, we can expect to see a characteristic pattern of mutations caused by the hereditary disorder. We cloned a cell by generating an iPS cell line and performed a whole-exome sequencing analysis of the progenitor and its iPS cell lines. Unexpectedly, we failed to find causal mutations in the XP-related genes, but we identified many other mutations including homozygous deletion of *GSTM1* and *GSTT1*. In addition, we found that the long arm of chromosome 9 formed uniparental disomy in the iPS cell line, which was also confirmed by a structural mutation analysis using a SNP array. Type and number of somatic mutations were different from those observed in XP patients. Taken together, we conclude that the patient might be affected by a different type of the disorder and that some of the mutations that we identified here may be responsible for exhibiting the phenotype. Sequencing and SNP-array data have been submitted to SRA and GEO under accession numbers SRP059858 and GSE55520, respectively.

Specifications	
Organism/cell line/tissue	*Homo sapiens*/XP40OS/fibroblast and its iPS cells
Sex	Male
Sequencer or array type	Illumina HiSeq 1000 and HumanCytoSNP-12
Data format	FASTQ and matrix tables
Experimental factors	Fibroblast and its iPS cells
Experimental features	Identification of somatic mutations using iPS-cell cloning
Consent	Publicly available from NCBI SRA and GEO
Sample source location	Japanese Collection of Research Bioresources (JCRB) Catalog No.: JCRB0327

1. Direct link to deposited data

http://www.ncbi.nlm.nih.gov/sra/?term=SRP059858
http://www.ncbi.nlm.nih.gov/geo/query/acc.cgi?acc=GSE55520
http://epigenetics.nrichd.ncchd.go.jp/ips/data/XP40OS.vcf.bz2
http://epigenetics.nrichd.ncchd.go.jp/ips/data/XP40OS.tsv.bz2

2. Experimental design, materials and methods

Xeroderma pigmentosum (XP) is caused by a deficiency in base excision repair, resulting in a large number of single-nucleotide mutations, especially in sun-exposed skin [1]. Due to the independent manner of the occurrence of the somatic mutations, the patient tissue, including fibroblasts, may form a high degree of mosaicism. If a mutation had occurred in an early stage of development or in stem cells, it could readily be detected by DNA sequencing. Most of the mutations that have occurred in skin cells would not be expanded much because the greater part of the cells is rather differentiated. Hence, it seems difficult to obtain a genome-wide pattern of XP-derived mutations. However, it may be possible to examine a whole set of mutations of a single cell if the cell could be cloned. This can be achieved by generation of iPS cells

* Corresponding author.
E-mail address: umezawa@1985.jukuin.keio.ac.jp (A. Umezawa).

http://dx.doi.org/10.1016/j.gdata.2015.07.008

owing to the fact that the process is cloning *per se* [2]. One may suspect that a number of *de novo* mutations arise during the reprogramming process and cultivation after the establishment of an iPS cell line, but many recent studies have demonstrated that most of the mutations found in iPS cells were preexisting in their progenitor lines, suggesting the high genetic stability of reprogramming and subsequent cultivation [3,4]. In the present study, we focused on a fibroblast cell line derived from an XP patient and established its iPS cell lines in order to delineate somatic mutations in the exome-target regions.

We obtained the XP40OS cell line, which was derived from a patient diagnosed with XP group C, from the JCRB Cell Bank [5]. This study was approved by the Institutional Review Board at the National Center for Child Health and Development. Employing the same method described in our previous study, we established its iPS cell line and performed whole-exome sequencing and structural alteration analyses for both the progenitor and iPS cell lines [6]. In brief, the iPS cells were generated by reprogramming with Sendai virus infection-mediated expression of the four factors. Extracted DNA samples were treated with Agilent SureSelect Human All Exon V4 + UTRs + lincRNA, whose target size was approximately 80 Mb, to prepare a pair-end library. The library was sequenced on the Illumina platform, yielding 18.8 Gb (93.3 M read pairs) and 18.7 Gb (92.7 M read pairs) data, respectively. After trimming, the data sizes were reduced to 16.9 Gb (84.3 M read pairs) and 16.8 Gb (83.7 M read pairs). For both samples, over 99% bases had q-scores that are more than 15. Our pipeline software included cutadapt-1.7.1, BWA 0.7.12, SAMtools 1.2, Picard 1.130, Genome Analysis Toolkit 3.3, and our own custom programs coded in C or Perl. Reads were mapped to the hs37d5 (GRCh37) reference sequence and PCR duplicate reads were then eliminated. Ratios of PCR duplicates were 27.4% and 26.5%, respectively. Along with in-house control data, multi-sample calling of single-nucleotide and short indel variations was performed. Filtration and identification of somatic mutations were carried out as described in our previous study [6].

First, we searched for possible variants that could affect the XP phenotype. Such variants should be found in both lines. A homozygous one (rs1800975) was found in the 5′ untranslated region of the *XPA* gene and two heterozygous ones (rs2228000 and rs2228001), which alter amino acid sequences, were found in the protein-coding regions of the *XPC* gene. Since their allelic frequencies in the population were not rare (50.8%, 32.6%, and 60.6%, respectively, according to the Human Genetic Variation Database, http://www.genome.med.kyoto-u.ac.jp/SnpDB), they cannot be considered as etiologic variants. While we failed to find any other notable variants in XP-related genes, we found homozygous deletions in the *BTNL3*, *GSTM1*, *GSTT1*, and *SLC25A24* loci. The *GSTM1* and *GSTT1* genes lacked the entire coding regions. The list of all possible variants is available from the websites (see the "Direct link to deposited data" section).

Next, we searched for inconsistent genotypes called with UnifiedGenotyper between the progenitor and its iPS cell lines to identify somatic mutations. Using the criteria described in our previous study [6], 922 single-nucleotide substitutions and 77 indels were identified. Because the numbers were extremely high compared to those of the preceding studies, we examined the positions of all the genotypes that exhibited disagreement between the two lines (Fig. 1). Among these sites, 845 single-nucleotide and 69 indel sites were located on the long arm of chromosome 9. All the called genotypes were homozygous without exception. Using an Illumina HumanCytoSNP-12 v2.1 DNA Analysis BeadChip Kit, we also performed a SNP-genotyping analysis to examine the existence of structural alterations. Copy-neutral loss of heterozygosity was detected in the 9:71,035,938–138,893,874 region (GRCh37) of the iPS cell line, indicating that a large structural mutation formed uniparental disomy. In that case, heterozygous sites in the region became homozygous. The 914 sites in the exome-target regions were considered to be just heterozygous in the progenitor cell, but not individual mutations. The SNP-genotyping analysis also suggested one copy-gain mutation around 16:83,939,438–85,567,156 only in the iPS cell line, but no genotype disagreement was found in this 1.6-Mb region. Among the remaining 77 single-nucleotide substitutions, C-to-T or G-to-A transitions accounted for 29 of the changes.

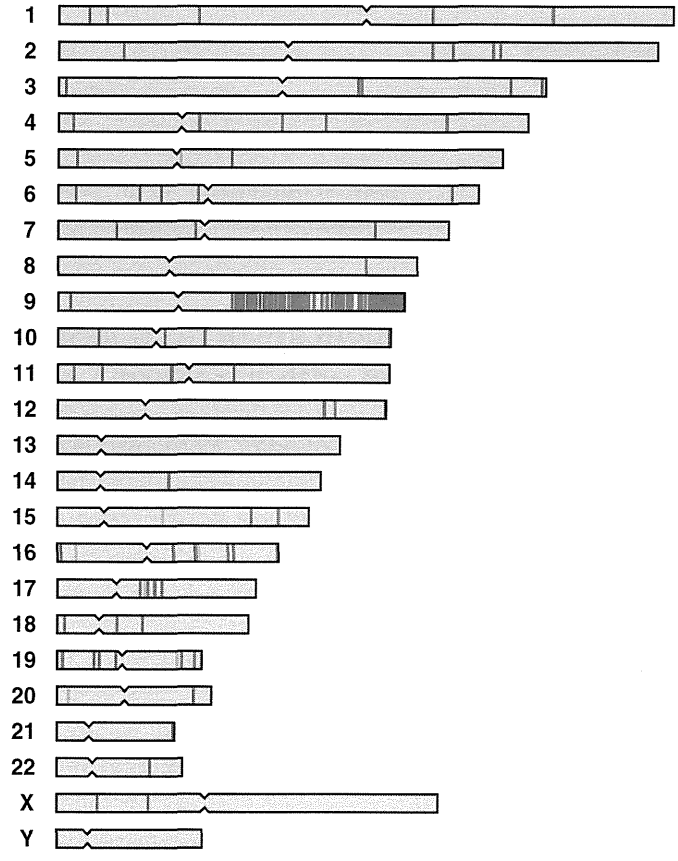

Fig. 1. Genome-wide distribution of the somatic mutations identified in the present study. Blue and red bars indicate single-nucleotide and indel mutations, respectively. Nearly one thousand mutations were detected on the long arm of chromosome 9. The discrepant genotypes between the progenitor and its iPS cell lines were caused by a single structural mutation that formed uniparental disomy in the chromosome arm.

3. Discussion

It is well known that C-to-T or G-to-A transitions in a dipyrimidine context are typical type of UV-specific mutations [7]. A trinucleotide analysis revealed that TCT, TCC, TCA, and their complementary trinucleotides, in which the mutated base is situated in the center, are frequently subject to mutation. Partially due to the relatively low number of mutations, the significance of the mutation type in the sample was not determined. In addition to the fact that we failed to find crucial mutations in XP-related genes in the exome-target regions, the donor of the fibroblast might be affected by another type of XP. It could be possible that some of the mutations that we identified in both of the lines are responsible for the phenotype.

Conflict of interest

The authors declare that there are no conflicts of interests.

Acknowledgements

We would like to express our sincere thanks to Dr. C. Ketcham for English editing and to E. Suzuki and K. Saito for secretarial work. This research is (partially) supported by the Research Project for Practical Applications of Regenerative Medicine (15bk0104028h0003) from Japan Agency for Medical Research and development, AMED. We acknowledge the International High Cited Research Group (IHCRG #14-104), Deanship of Scientific Research, King Saud University,

Riyadh, Kingdom of Saudi Arabia. AU thanks King Saud University, Riyadh, Kingdom of Saudi Arabia, for the Visiting Professorship. Computation time was provided by the computer cluster Hitachi HA8000/RS210 at the Center for Regenerative Medicine, National Research Institute for Child Health and Development.

References

[1] L. Li, E.S. Bales, C.A. Peterson, R.J. Legerski, Characterization of molecular defects in xeroderma pigmentosum group C. Nat. Genet. 5 (4) (1993) 413–417.
[2] S. Yamanaka, Elite and stochastic models for induced pluripotent stem cell generation. Nature 460 (7251) (2009) 49–52.
[3] A. Gore, Z. Li, H.L. Fung, J.E. Young, S. Agarwal, J. Antosiewicz-Bourget, I. Canto, A. Giorgetti, M.A. Israel, E. Kiskinis, J.H. Lee, Y.H. Loh, P.D. Manos, N. Montserrat, A.D. Panopoulos, S. Ruiz, M.L. Wilbert, J. Yu, E.F. Kirkness, J.C. Izpisua Belmonte, D.J. Rossi, J.A. Thomson, K. Eggan, G.Q. Daley, L.S. Goldstein, K. Zhang, Somatic coding mutations in human induced pluripotent stem cells. Nature 471 (7336) (2011) 63–67.
[4] M.A. Young, D.E. Larson, C.W. Sun, D.R. George, L. Ding, C.A. Miller, L. Lin, K.M. Pawlik, K. Chen, X. Fan, H. Schmidt, J. Kalicki-Veizer, L.L. Cook, G.W. Swift, R.T. Demeter, M.C. Wendl, M.S. Sands, E.R. Mardis, R.K. Wilson, T.M. Townes, T.J. Ley, Background mutations in parental cells account for most of the genetic heterogeneity of induced pluripotent stem cells. Cell Stem Cell 10 (5) (2012) 570–582.
[5] K. Sato, M. Ikenaga, S. Sano, Kinetic analysis of polyethylene glycol-induced cell fusion in cultured human fibroblasts: its application to genetic complementation analysis of xeroderma pigmentosum. Med. J. Osaka Univ. 33 (1–2) (1982) 19–28.
[6] Y. Fukawatase, M. Toyoda, K. Okamura, K. Nakamura, K. Nakabayashi, S. Takada, M. Yamazaki-Inoue, A. Masuda, M. Nasu, K. Hata, K. Hanaoka, A. Higuchi, K. Takubo, A. Umezawa, Ataxia telangiectasia derived iPS cells show preserved x-ray sensitivity and decreased chromosomal instability. Sci. Rep. 4 (2014) 5421.
[7] D.E. Brash, J.A. Rudolph, J.A. Simon, A. Lin, G.J. McKenna, H.P. Baden, A.J. Halperin, J. Pontén, A role for sunlight in skin cancer: UV-induced p53 mutations in squamous cell carcinoma. Proc. Natl. Acad. Sci. U. S. A. 88 (22) (1991) 10124–10128.

SCIENTIFIC REPORTS

OPEN

Long-term xeno-free culture of human pluripotent stem cells on hydrogels with optimal elasticity

Received: 19 August 2015
Accepted: 13 November 2015
Published: 14 December 2015

Akon Higuchi[1,2,3,4], Shih-Hsuan Kao[1], Qing-Dong Ling[5,6], Yen-Ming Chen[1], Hsing-Fen Li[1], Abdullah A. Alarfaj[4], Murugan A. Munusamy[4], Kadarkarai Murugan[7], Shih-Chang Chang[8], Hsin-Chung Lee[8,9], Shih-Tien Hsu[10], S. Suresh Kumar[11] & Akihiro Umezawa[2]

The tentative clinical application of human pluripotent stem cells (hPSCs), such as human embryonic stem cells and human induced pluripotent stem cells, is restricted by the possibility of xenogenic contamination resulting from the use of mouse embryonic fibroblasts (MEFs) as a feeder layer. Therefore, we investigated hPSC cultures on biomaterials with different elasticities that were grafted with different nanosegments. We prepared dishes coated with polyvinylalcohol-co-itaconic acid hydrogels grafted with an oligopeptide derived from vitronectin (KGGPQVTRGDVFTMP) with elasticities ranging from 10.3 to 30.4 kPa storage moduli by controlling the crosslinking time. The hPSCs cultured on the stiffest substrates (30.4 kPa) tended to differentiate after five days of culture, whereas the hPSCs cultured on the optimal elastic substrates (25 kPa) maintained their pluripotency for over 20 passages under xeno-free conditions. These results indicate that cell culture matrices with optimal elasticity can maintain the pluripotency of hPSCs in culture.

Human pluripotent stem cells (hPSCs), such as human embryonic stem cells (hESCs)[1] and induced pluripotent stem cells (hiPSCs)[2,3], are a promising cell source for regenerative medicine, disease modeling, and drug screening because they can differentiate into specialized cells that originate from all three germ layers[4–6]. The development of a fully defined and xeno-free microenvironment for hPSC culture is necessary for the use of hPSCs in cell therapy and tissue engineering. The current gold standards for maintaining hPSCs in a pluripotent (undifferentiated) state are: (a) culture on feeder cells such as mouse embryonic fibroblasts (MEFs) or human fibroblasts and (b) culture on Matrigel or Geltrex[7,8]. Because Matrigel and Geltrex are extracted from the sarcomas of Engelbreth-Holm-Swarm mice, both gold standard hPSC culture systems are undefined; therefore their xenogenic components hinder the clinical application of hPSCs.

There is a need to develop cell biomaterials for feeder-free and xeno-free conditions for the expansion of hPSCs for clinical applications. Recently, several cell culture matrices that are chemically defined and devoid of xenogenic components have been developed for hPSC culture to maintain their pluripotency. The design of these cell culture matrices is based on the introduction of biological cues, such as extracellular matrices (ECMs)[9–24], oligopeptides derived from ECMs[25–38], and completely synthetic organic molecules[39–45], on cell culture dishes.

[1]Department of Chemical and Materials Engineering, National Central University, No. 300 Jhongli, Taoyuan, 32001 Taiwan. [2]Department of Reproduction, National Research Institute for Child Health and Development, 2-10-1 Okura, Setagaya-ku, Tokyo 157-8535, Japan. [3]Nano Medical Engineering Laboratory, RIKEN, 2-1, Hirosawa, Wako, Saitama 351-0198, Japan. [4]Department of Botany and Microbiology, College of Science, King Saud University, P.O. Box 2455, Riyadh 11451, Saudi Arabia. [5]Cathay Medical Research Institute, Cathay General Hospital, No. 32, Ln 160, Jian-Cheng Road, Hsi-Chi City, Taipei, 221, Taiwan. [6]Graduate Institute of Systems Biology and Bioinformatics, National Central University, No. 300, Jhongda RD., Jhongli, Taoyuan, 32001 Taiwan. [7]Division of Entomology, Department of Zoology, School of Life Sciences, Bharathiar University, Coimbatore, Tamil Nadu, India. [8]Department of Surgery, Cathay General Hospital, No.280, Sec. 4, Ren'ai Rd., Da'an Dist., Taipei, 10693, Taiwan. [9]Graduate Institute of Translational and Interdisciplinary Medicine, College of Health Science and Technology, National Central University, No. 300, Jhongda RD., Jhongli, Taoyuan, 32001 Taiwan. [10]Department of Internal Medicine, Taiwan Landseed Hospital, 77, Kuangtai Road, Pingjen City, Taoyuan 32405, Taiwan. [11]Department of Medical Microbiology and Parasitology, Universities Putra Malaysia, Serdang 43400, Slangor, Malaysia. Correspondence and requests for materials should be addressed to A.H. (email: higuchi@ncu.edu.tw) or S.S.K. (email: sureshkudsc@gmail.com)

Dishes coated with recombinant extracellular matrices (ECMs) such as recombinant vitronectin, laminin (laminin-511, laminin-521 and laminin-322), and fibronectin (CellStart) showed excellent performance for hPSC cultures in chemically defined and/or serum-containing media[9–24]. Dishes immobilized with oligopeptides derived from ECMs were also reported to maintain hPSC pluripotency in chemically defined medium[25–38]. Completely synthetic dishes, such as PMVE-alt-MA (poly(methyl vinyl ether-alt-maleic anhydride)[39]), PMEDSAH (poly[2-(methacryloyloxy](ethyldimethyl-(3-sulfopropyl)ammoniumhydroxide[40–43]), APMAAm (aminopropylmethacrylamide[44]) and copoly(AEtMA-co-DEAEA) (copoly[2-(acryloyloxyethyl)] trimethylammonium-co-2-(diethylamino)ethyl acrylate][45]), have been also developed for hPSC culture in chemically defined medium, although there are no cell binding sites on the surfaces of the synthetic dishes. Therefore, it is necessary to evaluate the mechanism of pluripotent maintenance of hPSCs on synthetic dishes.

Increasing evidence suggests that both the physical cues (i.e., elasticity (stiffness)) and biological cues from the cell culture biomaterials direct stem cell fate during proliferation and maintain their pluripotency and differentiation[46,47]. Human mesenchymal stem cells (hMSCs) tend to efficiently differentiate into specific lineages of cells when they are grown on biomaterials with an elasticity similar to the tissue of interest[46]. Engler *et al.* demonstrated that hMSCs cultured on soft substrates (with elastic properties similar to brain tissue) in expansion media differentiated spontaneously into early lineages of neural cells, while hMSCs cultured on substrates with elastic moduli similar to muscle and bone tissue differentiated into early lineages of myocytes and osteoblasts, respectively[46]. These effects were explained by the ability of hMSCs to spread across biomaterials and form cytoskeletal stress fibers. Importantly, the effect of elasticity in cell culture biomaterials on the differentiation fate of hMSCs is restricted to the early stages of differentiation and does not direct the mature differentiation stages of hMSCs[47,48]. Furthermore, there are some contradictory reports[47,49,50] for this well-known finding reported by Engler *et al.*[47] However, the physical cues produced by biomaterials during the proliferation or differentiation of hPSCs into specific cell lineages should be an important contributing factor for the design of cell culture biomaterials for stem cell proliferation and differentiation[47].

The microenvironment has also been reported to dictate the consequences of hPSCs[7,8]. Chowdhury *et al.* reported that mouse ESCs (mESCs) could maintain pluripotency when cultured in the absence of exogenous leukemia inhibitory factor (LIF) on soft substrates (0.6 kPa) that matched the intrinsic stiffness of mESCs, whereas mESCs did not maintain pluripotency in conventional stiff culture polystyrene dishes (12 GPa) coated with collagen type I or on hydrogels with much stiffer moduli[51].

Several notable investigations addressed the effects of the elasticity of cell culture biomaterials on the pluripotency and differentiation fates of hMSCs and mESCs[46–48,51]. However, little is known about the effect of elasticity of the biomaterials on the pluripotency fate and proliferation of hESCs. This lack of evidence motivated us to investigate the effect of the elasticity of hydrogels grafted with biologically active nanosegments on hPSCs.

In this study, we developed synthetic hydrogels consisting of poly(vinyl alcohol-co-itaconic acid) (PVA-IA) grafted with oligopeptides derived from vitronectin (oligoVN) to evaluate the physical effect of substrate stiffness on the pluripotency and proliferation fates of hESCs and hiPSCs. These hydrogels were prepared with different elasticities by controlling the crosslinking intensity (time) with glutaraldehyde. The elasticity of the PVA-IA hydrogels could be varied using the same chemical structure as the polymeric main chain with different crosslinking intensities. OligoVN could be spontaneously grafted with the carboxylic acid group of PVA-IA via N-(3-dimethylaminopropyl)-N'-ethylcarbodiimide hydrochloride (EDC) and N-hydroxysuccinimide (NHS) chemistry in an aqueous solution. PVA-IA hydrogels grafted with or without oligoVN were transparent, thereby allowing the evaluation of the morphology of hSPCs cultured on the PVA-IA hydrogels using microscopy techniques similar to those employed using conventional cell culture dishes. The goal of this study is to investigate the optimal elasticity of PVA-IA hydrogels grafted with oligoVN for the expansion of hSPCs in xeno-free medium for a long period of time (at least 20 passages).

Results

Physical characterization of PVA-IA hydrogel dishes. PVA-IA hydrogels grafted with oligoVN with different elasticities were prepared to investigate the optimal culture dish elasticity for hPSC expansion. The elasticity of PVA-IA hydrogels was controlled by the applied glutaraldehyde crosslinking intensity (time) (Fig. 1A). PVA-IA films with a $1.5 \pm 0.3\,\mu m$ thickness under dry conditions were used for these experiments. The thickness of the PVA-IA films (hydrogels) in the dishes in water was evaluated with a microgauge and determined to be 2.2–2.9 μm. The storage modulus *E'* of self-standing PVA-IA hydrogels with a thickness of approximately 20–30 μm was also measured using a rheometer. The softest PVA-IA hydrogel included in this study (PVA-1h) had an *E'* of 10.3 kPa, whereas the *E'* of the hardest PVA-IA hydrogel in this study (PVA-48h) was 30.4 kPa, nearly 3-fold higher than the *E'* of PVA-1h (Fig. 2A). The *E'* of PVA-6h, PVA-12h, and PVA-24h hydrogels in this study was 15.8 kPa, 21.2 kPa, and 25.3 kPa, respectively (Fig. 2A). The storage moduli of PVA-IA hydrogels grafted with oligoVN were found to be approximately the same as those of the unmodified PVA-IA hydrogels within the range of experimental error, because the amount of oligoVN grafting was too small to contribute to the *E'* of the bulk PVA-IA hydrogels.

Analysis of the chemical surface of PVA-IA dishes grafted with oligoVN. It is important to evaluate the existence of nanosegments (i.e., oligoVN) and the surface density of the nanosegments on PVA-IA hydrogels grafted with oligoVN that have different elasticities. However, determining the absolute quantity of grafted nanosegments on PVA-IA hydrogels via colorimetric (e.g., microBCA) or other chemical titration and reaction methods in this study was extremely difficult. Furthermore, the absolute quantity of nanosegments grafted onto the surface could not be evaluated using an ELISA (enzyme-linked immunosorbent assay) method. Therefore, we analyzed the surface of PVA-IA hydrogels grafted with or without oligoVN via XPS (X-ray photoelectron spectroscopy). Figure 1B provides the high-resolution XPS spectra of the C1s and N1s peaks on unmodified PVA-IA dishes (PVA-24h) and PVA-IA dishes grafted with oligoVN (PVA-24h-1000).

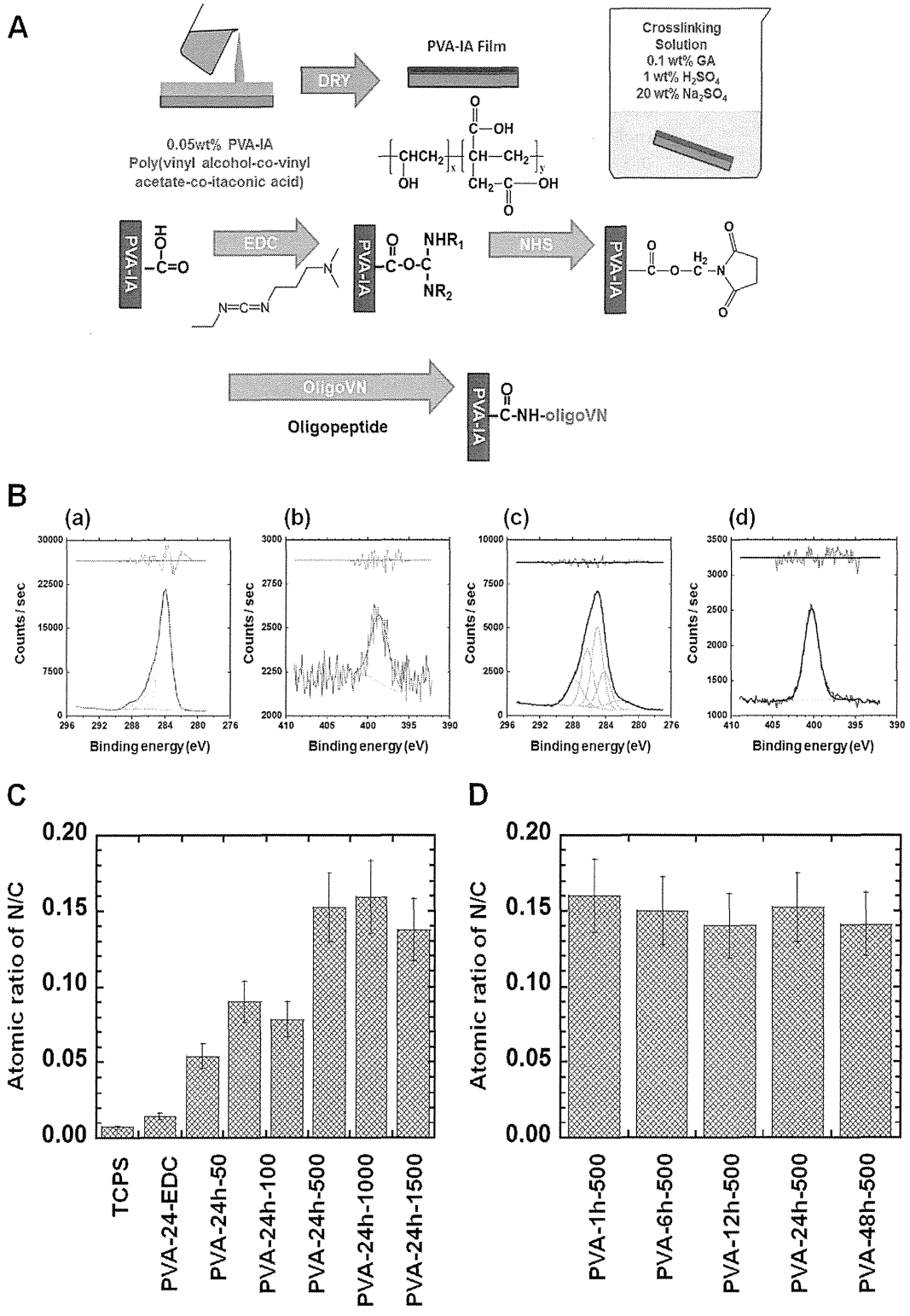

Figure 1. Preparation and characterization of PVA-IA hydrogels grafted with oligoVN. (**A**) Reaction scheme for PVA-IA hydrogels grafted with oligoVN. (**B**) High-resolution XPS spectra of the C1s (a and c) and N1s (**b** and **d**) peaks obtained on the surface of unmodified PVA-24h (a and b) and PVA-24h-1000 (c and d) dishes. (**C**) The atomic ratios of nitrogen to carbon (N/C) in TCPS, PVA-24h-EDC, and PVA-24h hydrogels grafted with different concentration of oligoVN (PVA-24h-50, PVA-24h-100, PVA-24h-500, PVA-24h-1000, and PVA-24h-1500). (**D**) The atomic ratios of nitrogen to carbon (N/C) in PVA-24h hydrogels grafted with different reaction time of oligoVN (PVA-1h-500, PVA-6h-500, PVA-12h-500, PVA-24h-500, and PVA-48h-1500).

C–N bonding (285.9 eV), O–C = O bonding (289.3 eV), and C–C and C–H bonding (285.0 eV) were clearly observed in the XPS spectra obtained for the PVA-24h-1000 dishes (Fig. 1B(c)) compared to the PVA-24h dishes (Fig. 1B(a)). In contrast, C–C and C–H bonding (285.0 eV) were mainly observed in the XPS spectra of the PVA-24h dishes (Fig. 1B(a)). These findings suggest that oligoVN is covalently conjugated in the PVA-IA hydrogels.

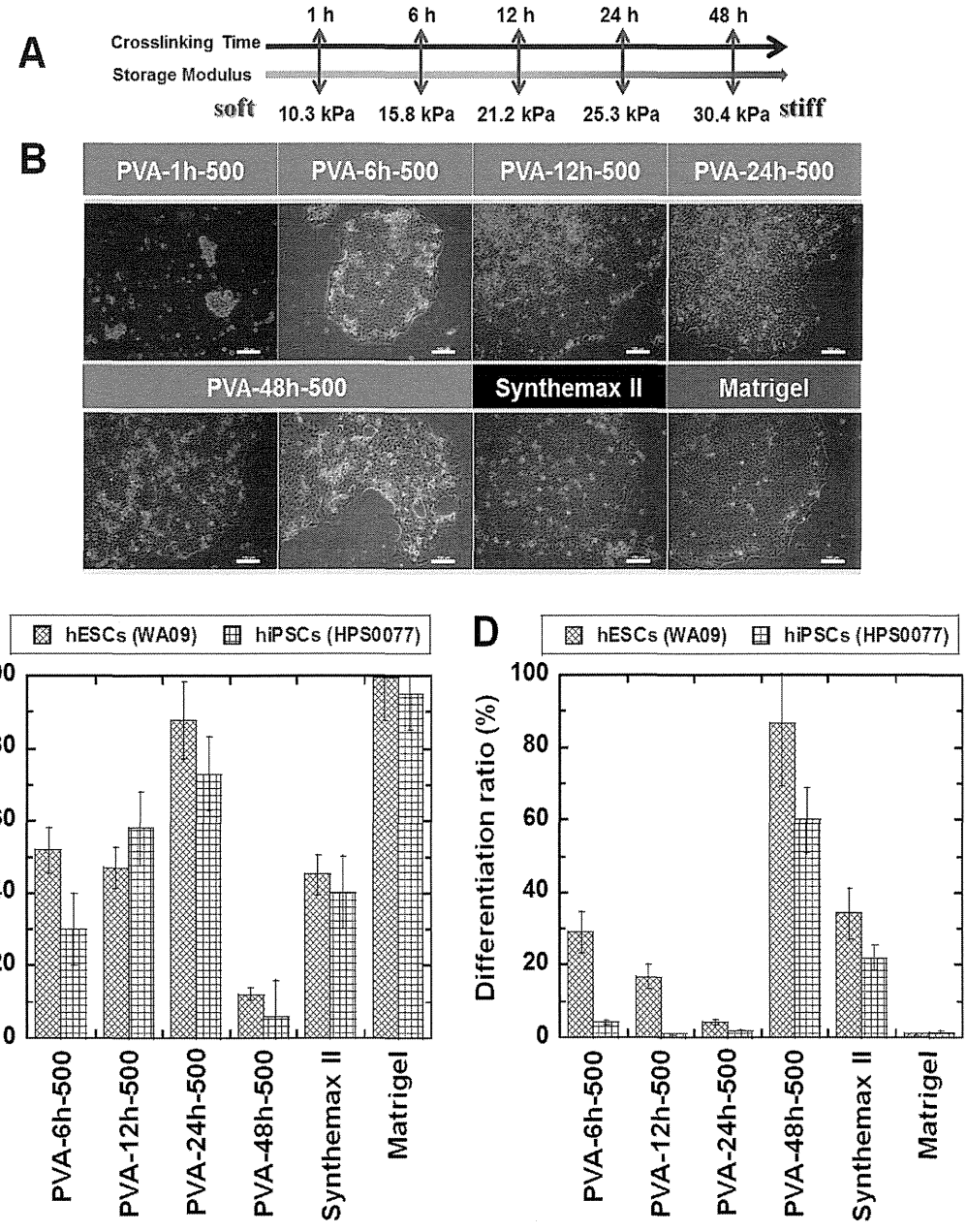

Figure 2. hPSC culture on PVA-oligoVN hydrogels with optimal elasticity. (**A**) Elasticity (storage modulus) is regulated by the crosslinking time on PVA-oligoVN hydrogels. (**B**) Morphology of hESCs (WA09) cultured on PVA-oligoVN hydrogels with several elasticities (PVA-1h-500, PVA-6h-500, PVA-12h-500, PVA-24h-500, and PVA-48h-500), Synthemax II dishes, and Matrigel at passage 1. The bar indicates 100 μm. (**C**) Attachment ratio of PSCs (blue bar, hESCs [WA09] and red bar, hiPSCs [HPS0077]) on PVA-oligoVN hydrogels with several elasticities, Synthemax II dishes, and Matrigel at passage 3. (**D**) Differentiation ratio of hPSCs (blue bar, hESCs [WA09] and red bar, hiPSCs [HPS0077]) on PVA-oligoVN hydrogels with several elasticities, Synthemax II dishes, and Matrigel at passage 3.

The high-resolution XPS spectra of the N1s peaks obtained for the unmodified PVA-IA (PVA-24h, Fig. 2B(b)) and PVA-24h-1000 (Fig. 1B(d)) dishes were evaluated. An N1s peak at 399 eV[52] was clearly observed in the PVA-24h-1000 dishes (Fig. 1B(d)). Conversely, only a faint N1s peak at 399 eV was found in the unmodified PVA-24h dishes (Fig. 1B(b)) due to the fact that PVA-IA does not initially include molecules containing nitrogen atoms; instead, nitrogen atoms can be derived from proteins and oligopeptides (i.e., oligoVN).

The atomic ratios of N/C on the PVA-24h dishes activated by EDC/NHS (PVA-24h-EDC) and the PVA-24h-oligoVN dishes were determined from the XPS spectra and shown in Fig. 1C. The N/C ratios of tissue culture polystyrene (TCPS, negative control) and PVA-24h-EDC were minimal. The N/C ratio increased with the increasing concentration of oligoVN used for grafting on the PVA-24h-oligoVN dishes up to 500 μg/ml, whereas the N/C ratio of PVA-24h-oligoVN reacted with concentrations of oligoVN $\geq$ 500 μg/ml were approximately the same within experimental error. This result indicates that the surface density of oligoVN grafted onto the PVA-IA hydrogels becomes saturated when the concentration of oligoVN is greater than 500 μg/ml.

The N/C ratios of PVA-IA hydrogels grafted with 500 μg/ml of oligoVN with different elasticities was also investigated (Fig. 1D). The N/C ratios of PVA-IA hydrogels grafted with the same concentration of oligoVN was approximately the same as PVA-IA hydrogels with different elasticities (i.e., PVA-1h-500, PVA-6h-500, PVA-12h-500, PVA-24h-500 and PVA-48h-500 dishes). This result is because the same concentration of oligoVN was used to graft onto the PVA-IA hydrogels. Thus, the surface density of oligoVN grafted onto PVA-IA hydrogels with different elasticities prepared with the same concentration of oligoVN is expected to be the same.

hPSC culture on PVA-oligoVN hydrogels with optimal elasticity. hPSCs were cultured on PVA-oligoVN hydrogels with different elasticities to evaluate the effect of the elasticity of the hydrogels on the expansion of hPSCs and their ability to maintain their pluripotency. The first screening to evaluate biomaterials for hPSC culture is to evaluate the attachment of hPSCs and investigate the morphology of hPSC colonies showing no differentiation, because hPSCs cultured on adequate biomaterials show good attachment and colony morphology shapes that are characteristic of hPSCs. Figure 2B shows the morphology of hESCs (WA09) cultured on PVA-oligoVN dishes with several elasticities (PVA-1h-500, PVA-6h-500, PVA-12h-500, PVA-24h-500, and PVA-48h-500 dishes) and dishes coated with commercially available Synthemax II (Synthemax II dishes) at passage 1. hESCs did not attach well on the soft PVA-1h-500 dishes, whereas hESCs attached well on the PVA-IA dishes with elasticities greater than 15 kPa (i.e., the PVA-6h-500, PVA-12h-500, PVA-24h-500, and PVA-48h-500 dishes). This result indicates that the minimum elasticity of the biomaterials is necessary to allow the attachment of hESCs to the biomaterials.

The attachment ratio of hPSCs cultured on PVA-oligoVN hydrogels, Synthemax II dishes and Matrigel was evaluated by microscopy at each passage; the results at passage 3 are shown in Fig. 2C. A high attachment ratio of hESCs (WA09) and hiPSCs (HPS0077) was observed on Matrigel and PVA-24h-500 dishes, whereas middle and low attachment ratios of hPSCs were found on the PVA-6h-500, PVA-12h-500, PVA-48h-500, and Synthemax II dishes. This result indicates that PVA-oligoVN hydrogels with optimal elasticity (PVA-24h-500, 25.3 kPa) show the highest attachment ratio among the PVA-oligoVN hydrogels. Synthemax II dishes showed a lower attachment ratio compared to the PVA-24h-500 dishes ($p < 0.05$) and a similar attachment ratio compared to hPSCs on the PVA-12h-500 dishes ($p > 0.05$).

hPSC pluripotency can be evaluated based on colony morphology and live staining of alkali phosphatase. Supplementary Figure 1 shows the hESC morphology of completely differentiated cells (a), partially differentiated cells (b), and pluripotent cells (c). No alkali phosphatase activity was detected in the completely differentiated cells (a). In contrast, while the edge of the colony of the partially differentiated cells did not exhibit alkali phosphatase activity, alkali phosphatase activity was detected in the center of the colony (b). The pluripotent cells exhibited good colony morphology and alkali phosphatase activity in most cells (c). The differentiation ratio was evaluated for the whole hPSC colony on the dishes and calculated using the following equation:

$$\begin{aligned}\text{Differentiation ratio}(\%) &= \text{Percentage of differentiated cells}(\%) \\ &+ \text{percentage of partially differentiated cells} \times 0.5(\%) \end{aligned} \quad (1)$$

The differentiation ratios of hPSCs cultured on PVA-oligoVN hydrogels, Synthemax II dishes and Matrigel were evaluated based on microscopy at each passage; the results at passage 3 are shown in Fig. 2D. Low hPSC differentiation ratios were observed on the PVA-24h-500 dishes and Matrigel, whereas relatively high differentiation ratios were observed on the PVA-48h-500 and Synthemax II dishes. This result also suggests that the optimal elasticity of cell culture biomaterials is necessary to maintain pluripotency (e.g., 25.3 kPa) when hPSCs are cultured on PVA-oligoVN hydrogels. Based on the hPSC attachment and differentiation ratios, the optimal elasticity of PVA-oligoVN hydrogels was defined as 25.3 kPa in this study. A higher attachment ratio and higher pluripotency (lower differentiation ratio) of hPSCs were achieved on PVA-24h-500 dishes compared with the commercially available Synthemax II dishes ($p < 0.05$).

Effect of oligoVN surface density on hPSC culture. The optimal elasticity of PVA-oligoVN hydrogels for hPSC culture was evaluated to be 25.3 kPa (crosslinking time = 24 h) in the previous section. Next, the effect of the oligoVN surface density in PVA-oligoVN hydrogels on hPSC culture was investigated in the following experiments. The surface density of oligoVN was controlled by its concentration (50–1500 μg/ml) in the solution that was reacted with the PVA-24-EDC hydrogels. Figure 3A shows hESC (WA009) morphology after culture on PVA-oligoVN with variable oligoVN surface densities (PVA-24h-50, PVA-24h-100, PVA-24h-250, PVA-24h-500, PVA-24h-1000, and PVA-24h-1500 dishes), Synthemax II dishes and Matrigel at passage 1. hPSCs were found to detach easily from the PVA-oligoVN hydrogels prepared using oligoVN concentrations less than 500 μg/ml. Additionally, hPSCs could not be cultured on PVA-24h-50 dishes for more than two passages. The attachment ratio of hESCs (WA09) and hiPSCs (HPS0077) on each of the PVA-oligoVN hydrogels, Synthemax II dishes and Matrigel was evaluated at each passage until passage 10; the results at passage 3 are shown in Fig. 3B. The attachment ratio of hPSCs increased with increasing concentrations of oligoVN reacted with PVA-24h-EDC until the concentration reached 500 μg/ml. The attachment ratio of hPSCs on the PVA-24h-500 dishes was found to be higher compared to the PVA-24h-250 dishes ($p < 0.05$). The attachment ratio of hPSCs on the PVA-24h-500, PVA-24h-1000, and PVA-24h-1500 dishes was almost the same within the experimental error ($p > 0.05$). The attachment ratio of hPSCs on the PVA-24h-1500 dishes was found to be much higher than the Synthemax II dishes ($p < 0.05$) but slightly less than the Matrigel ($p < 0.05$).

To evaluate the maintenance of pluripotency of hPSCs cultured on PVA-oligoVN hydrogels, the differentiation ratios of hPSCs cultured on PVA-oligoVN hydrogels, Synthemax II dishes and Matrigel were evaluated using microscopy at each passage; the results at passage 3 are shown in Fig. 3C. An extremely low hPSC differentiation

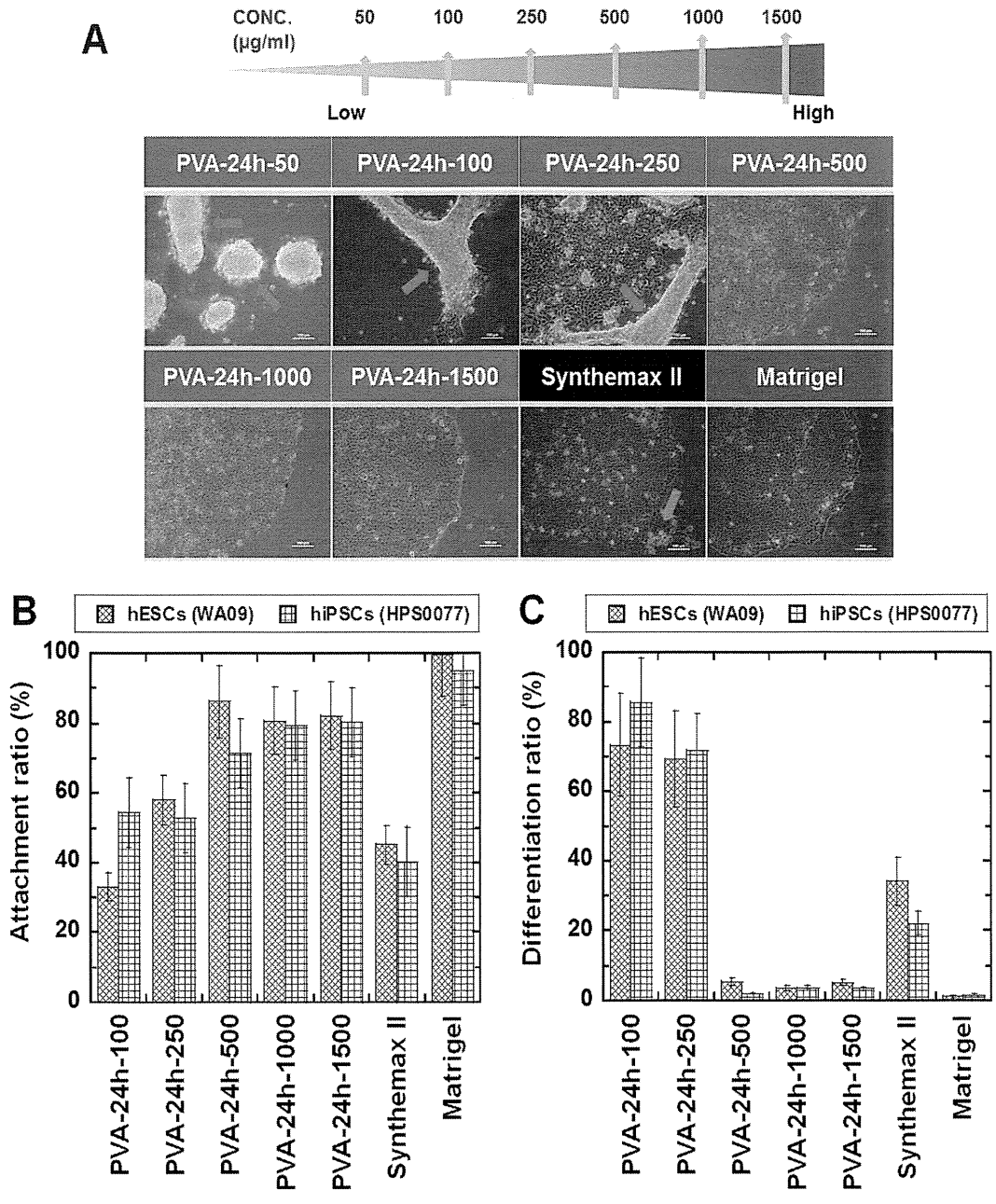

Figure 3. hPSC culture on PVA-oligoVN hydrogels with different surface densities of oligoVN. (**A**) Morphology of hESCs (WA09) cultured on PVA-oligoVN hydrogels with several surface densities of oligoVN (PVA-24h-50, PVA-24h-100, PVA-24h-250, PVA-24h-500, PVA-24h-1000, and PVA-24h-1500), Synthemax II dishes, and Matrigel at passage 1. The red arrows indicate detached cells. The bar indicates 100 μm. (**B**) Attachment ratio of hPSCs (blue bar, hESCs [WA09] and red bar, hiPSCs [HPS0077]) on PVA-oligoVN hydrogels with several surface densities of oligoVN, Synthemax II dishes, and Matrigel at passage 3. (**D**) Differentiation ratio of hPSCs (blue bar, hESCs [WA09] and red bar, hiPSCs [HPS0077]) on PVA-oligoVN hydrogels with several surface densities of oligoVN, Synthemax II dishes, and Matrigel at passage 3.

ratio was observed on the PVA-24h-500, PVA-24h-1000, and PVA-24h-1500 dishes and Matrigel, whereas a high differentiation ratio of hPSCs was observed on the PVA-24h-100 and PVA-24h-250 dishes and a relatively high differentiation ratio was found on the Synthemax II dishes. These results suggest that there is a threshold of oligoVN surface density (biological cues) on the PVA-oligoVN hydrogels that is needed to maintain hPSC pluripotency (i.e., low differentiation ratio). hPSCs attached to PVA-24h-oligoVN dishes prepared with more than 500 μg/ml of oligoVN and maintained their pluripotency to a level similar to that of cells cultured on Matrigel. It was necessary to use high concentration of oligoVN (500–1500 μg/ml) for the preparation of PVA-oligoVN hydrogels to maintain the pluripotency of hPSCs in this study. Active layer of Synthemax dishes is polyacrylate grafted with oligoVN and oligoVN used in Synthemax dishes is reported to be exactly the same sequence that we used for PVA-oligoVN hydrogels in this study[25]. High concentration of oligoVN such as 1 mM (1590 μg/ml) was reported to be used for the preparation of Synthemax dishes[25]. Therefore, it seems high concentration of oligoVN is necessary to keep pluripotency of hPSCs on the surface grafted with oligoVN.

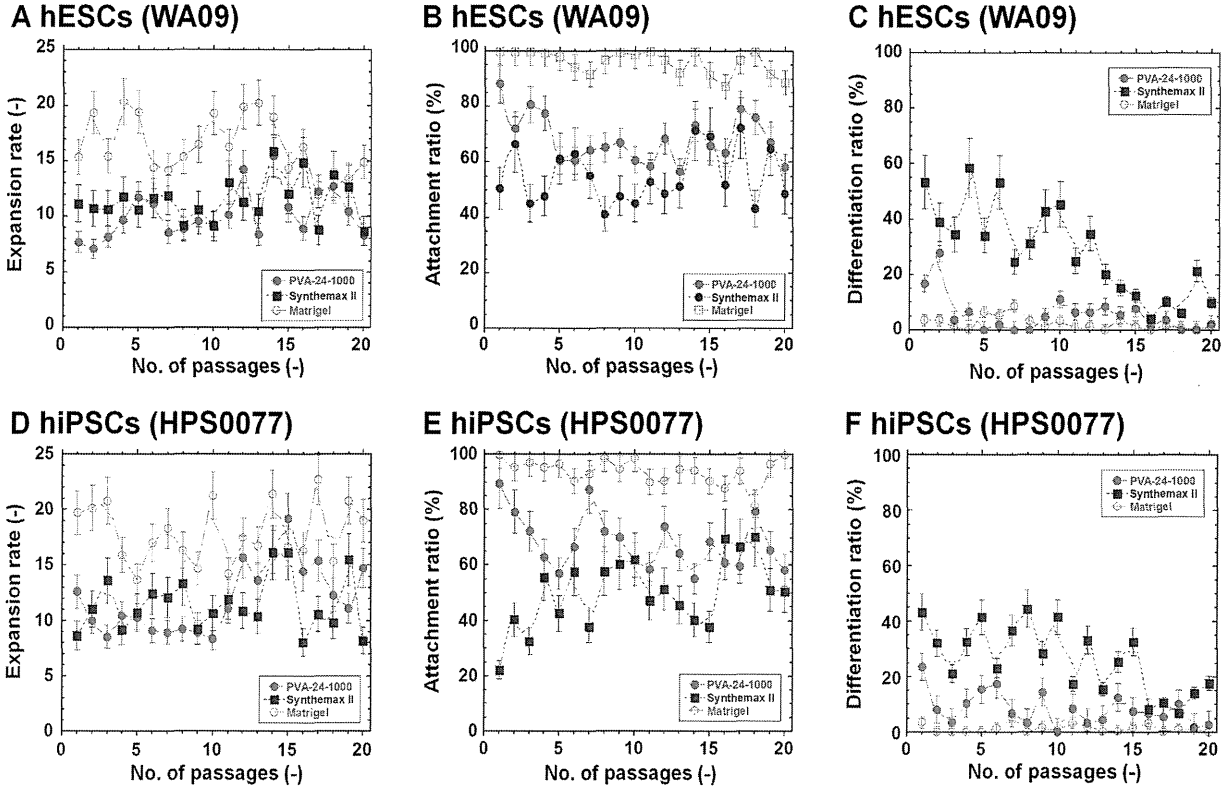

Figure 4. Long-term culture of hPSCs on PVA-oligoVN hydrogels with an optimal elasticity under xeno-free culture conditions. (**A**) Expansion rate of hESCs (WA09) on PVA-24h-1000 dishes (closed red circle), Synthemax II dishes (closed blue square), and Matrigel (open green circle) for 20 passages. (**B**) Attachment ratio of hESCs (WA09) on PVA-24h-1000 dishes (closed red circle), Synthemax II dishes (closed blue square), and Matrigel (open green circle) for 20 passages. (**C**) Differentiation ratio of hESCs (WA09) on PVA-24h-1000 dishes (closed red circle), Synthemax II dishes (closed blue square), and Matrigel (open green circle) for 20 passages. (**D**) Expansion rate of hiPSCs (HPS0077) on PVA-24h-1000 dishes (closed red circle), Synthemax II dishes (closed blue square), and Matrigel (open green circle) for 20 passages. (**E**) Attachment ratio of hiPSCs (HPS0077) on PVA-24h-1000 dishes (closed red circle), Synthemax II dishes (closed blue square), and Matrigel (open green circle) for 20 passages. (**F**) Differentiation ratio of hiPSCs (HPS0077) on PVA-24h-1000 dishes (closed red circle), Synthemax II dishes (closed blue square), and Matrigel (open green circle) for 20 passages.

Long-term culture of hPSCs under xeno-free culture conditions. We found that the PVA-24h-500, PVA-24h-1000, and PVA-24h-1500 dishes were suitable cell culture biomaterials for hPSC culture by optimizing the elasticity (physical cues) and fine-tuning the oligoVN surface density (biological cues) in the previous sections. Then, long-term culture (20 passages) of hPSCs was evaluated on one of the optimized PVA-oligoVN hydrogels (PVA-24h-1000) and Synthemax II dishes using the xeno-free culture medium Essential 8 (xeno-free medium) and compared to hPSCs cultured on Matrigel.

Figure 4 shows the expansion rate, attachment ratio, and differentiation ratio of hESCs (WA09) and hiPSCs (HPS0077) cultured on PVA-24h-1000 dishes for 20 passages compared to those cultured on Synthemax II and Matrigel. The fold expansion of hESCs and hiPSCs on the PVA-24h-1000 dishes was found to be almost the same as the cells grown on commercially available Synthemax II dishes but was slightly less than cells grown on Matrigel ($p < 0.05$). The attachment ratio of hESCs and hiPSCs on the PVA-24h-1000 dishes was slightly higher compared to the Synthemax II dishes during 20 passages, but the difference did not reach statistical significance ($p > 0.05$). However, when the time of hPSC culture was limited to be only early passages (i.e., less than 5 passages), the attachment ratio of hESCs and hiPSCs on the PVA-24h-1000 dishes was found to be higher compared to the Synthemax II dishes with statistically significance ($p < 0.05$). The attachment ratio of hESCs and hiPSCs on Matrigel was always greater than 80% during the 20 hPSC culture passages, which was significantly higher compared to the PVA-24h-1000 and Synthemax II dishes ($p < 0.05$). The differentiation ratio of hESCs and hiPSCs on the PVA-24h-1000 dishes and Matrigel was much lower compared to Synthemax II ($p < 0.05$), indicating that hESCs and hiPSCs can maintain pluripotency on the PVA-24h-1000 dishes and Matrigel for a long period of time (i.e., at least 20 passages).

These results indicate that hPSCs can be cultured on PVA-24h-1000 dishes and Synthemax II under feeder-free and xeno-free conditions, although hPSC cultures on Matrigel exhibited a better expansion rate and attachment ratio. However, the hPSC culture on the Matrigels was performed under xeno-containing conditions, whereas the hPSC culture on the PVA-24h-1000 and Synthemax II dishes was performed under xeno-free conditions that were preferable for future clinical applications. Furthermore, hPSC culture on the PVA-24h-1000 dishes was preferable to culture on the commercially available Synthemax II, especially at a lower differentiation ratio. Thus, hPSCs maintain higher pluripotency on the PVA-24h-1000 dishes compared to the Synthemax II dishes. This finding was also verified in the following experiments.

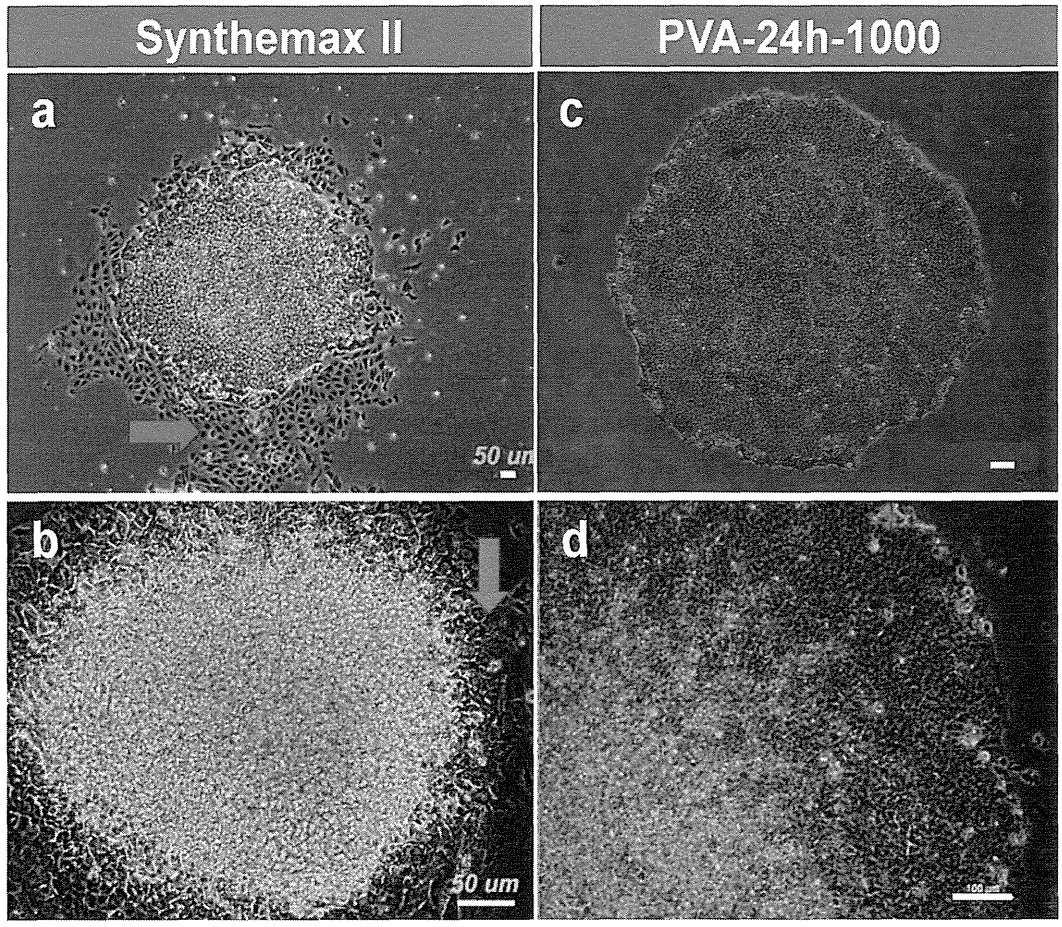

Figure 5. Comparison of hESC cultures on Synthemax II and PVA-oligoVN hydrogels. The morphology of hESCs (WA09) cultured on Synthemax II (**a,b**) and PVA-24h-1000 (**c,d**) dishes at passage 1 when hPSCs were shifted from culture on MEFs into culture on Synthemax II or PVA-24h-1000 dishes. Red arrows indicate differentiated hESCs. The bar indicates 50 μm (**a,b**) and 100 μm (**c,d**).

The results shown in Figs 2–4 were obtained using hPSCs cultured on Matrigel for nine passages in advance. This process is important for hPSCs to become accustomed to feeder-free conditions. We also performed hPSC cultures directly on Synthemax II and PVA-24-1000 dishes using hPSCs cultured on MEFs that were not cultured on Matrigel in advance; the results are shown in Fig. 5. hPSCs shifted directly to the Synthemax II dishes were found to more easily differentiate at passage one, whereas hPSCs could maintain pluripotency following direct transfer to the PVA-24h-1000 dishes. These results are consistent with those shown in Fig. 4C,F where the differentiation of hPSCs was more predominant on the Synthemax II dishes than on PVA-24h-1000 dishes.

hPSC pluripotency was evaluated based on the expression of pluripotent proteins on hESCs (WA09) and hiPSCs (HPS0077) by immunostaining after culturing on PVA-24h-1000 dishes for 20 passages; the results are shown in Fig. 6. The pluripotent proteins Oct3/4, Sox2, Tra-1-81, and SSEA-4 were expressed on hESCs and hiPSCs cultured on PVA-24h-1000 dishes under xeno-free conditions (i.e., in Essential 8 culture medium) for 20 passages.

Differentiation ability of hPSCs *in vivo* and *in vitro*. It is necessary to evaluate whether hPSCs can differentiate into cells derived from all three germ layers *in vitro* (EB formation assay) and *in vivo* (teratoma formation assay) to evaluate their pluripotency. hESCs (WA09) and hiPSCs (HPS0099) were cultured on PVA-24h-1000 dishes under xeno-free conditions for 20 passages and subsequently cultured in suspension using ultra low protein binding dishes to form EBs (Fig. 7A). Differentiated hESCs and hiPSCs were immunostained with AFP (alpha-fetoprotein, endoderm), SMA (smooth muscle actin, mesoderm), βIII-tubulin (ectoderm), and GFAP (glial fibrillary acidic protein, ectoderm); the results are shown in Fig. 7B for hESCs and Fig. 7C for hiPSCs. Both hESCs and hiPSCs were able to differentiate into cells expressing AFP, SMA, βIII-tubulin, and GFAP, indicating that the hESCs and hiPSCs could maintain their pluripotency after culture on PVA-24h-1000 dishes under xeno-free conditions and differentiate into cells derived from the three germ layers *in vitro*.

We evaluated the ability of hESCs to differentiate into cells derived from the three germ layers *in vivo* using the teratoma formation assay. hESCs cultured on PVA-24h-1000 dishes for ten passages were subcutaneously xenotransplanted into non-obese diabetic/severe combined immunodeficiency (SCID) mice to generate teratomas (Fig. 8). Staining the teratomas with hematoxylin and eosin (H&E) demonstrated the presence of cells derived from the three germ layers (enteron (endoderm), osteoblasts (mesoderm), chondrocytes (mesoderm), and neuron (ectoderm)). These results suggest that hPSCs cultured long-term on PVA-24h-1000 dishes (10–20 passages) can maintain their pluripotency and are able to differentiate into cells derived from the three germ layers *in vitro* and *in vivo*.

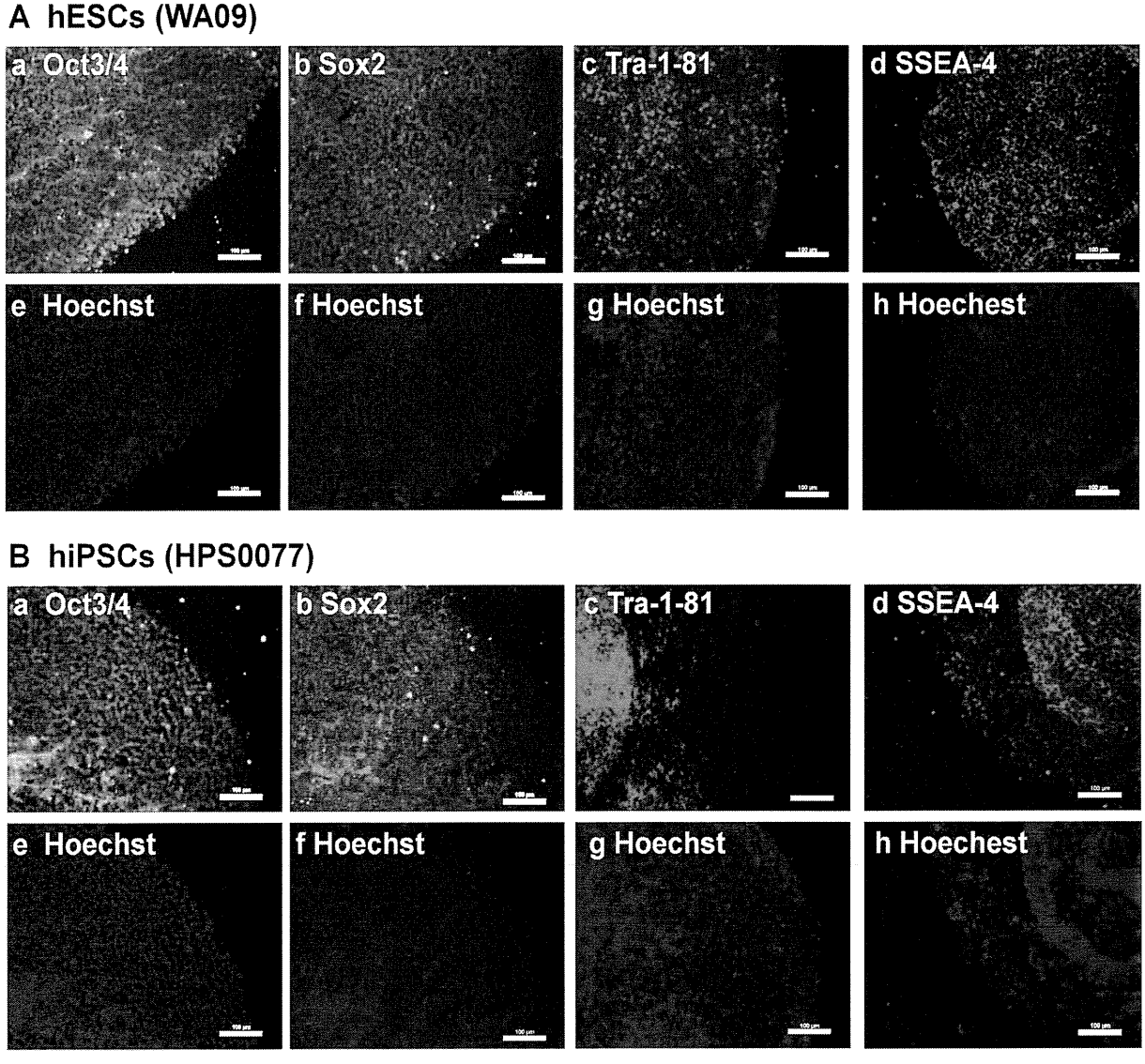

Figure 6. Characterization of pluripotency of hPSCs (hESCs and hiPSCs) cultured on PVA-oligoVN hydrogels based on expression of pluripotent proteins. (**A**) Pluripotent protein expression on hESCs (WA09) analyzed by immunostaining after culture on PVA-24h-1000 dishes under xeno-free conditions for 20 passages. (**a**) Oct3/4, (**b**) Sox2, (**c**) Tra-1-81, (**d**) SSEA-4 and (**e–h**) Hoechest staining of hESCs used in (**a–d**). The bar indicates 100 μm. (**B**) Pluripotent protein expression on hiPSCs (HPS0077) analyzed by immunostaining after culture on PVA-24h-1000 dishes under xeno-free conditions for 20 passages. (**a**) Oct3/4, (**b**) Sox2, (**c**) Tra-1-81, (**d**) SSEA-4 and (**e–h**) Hoechest staining of hESCs used in (**a–d**). The bar indicates 100 μm.

Discussion

Several hPSC culture substrates have been reported in feeder-free and chemically defined conditions. Some examples of hPSC culture substrates are briefly summarized in Table 1. Substrates coated or grafted with specific ECMs (fibronectin, laminin-511, laminin-521, laminin-332, and vitronectin)[9–24] and oligopeptides[25–38] derived from ECMs that have cell binding domains are typically used. Because the cost of production of ECMs originating from humans prepared under xeno-free conditions for good manufacturing practice (GMP) approval is high, hPSC culture substrates that immobilize ECM-derived oligopeptides represents a promising approach. Recently, completely synthetic polymers have been developed for use as hPSC culture substrates. For example, hPSCs can be cultured on APMAAm (aminopropylmethacrylamide), PMEDSAH (poly[2-(methacryloyloxy(ethyl dimethyl-(3-sulfopropyl) ammoniumhydroxide), and PMVE-alt-MA (poly[methyl vinyl ether-alt-maleic anhydride]) in chemically defined media[39–45]. However, hPSCs are cultured on Matrigel prior to culture on completely synthetic polymeric substrates, and Matrigel are derived under xeno-containing conditions. Furthermore, the mechanism of hPSC attachment to the completely synthetic polymer substrates is currently unknown. No systematic explanation for the molecular design of the synthetic polymer substrates based on hPSC attachment and proliferation has been reported. The other drawback of the use of completely synthetic polymeric substrates is that only polymer scientists and organic chemists can synthesize these types of complicated polymers, whereas ECMs and oligopeptides can be obtained commercially.

Currently, only coating materials and substrates are commercially available for hPSC culture substrates; these materials are composed of ECM-derived oligopeptides (with the exception of ECMs and chimeric proteins)[53,54].

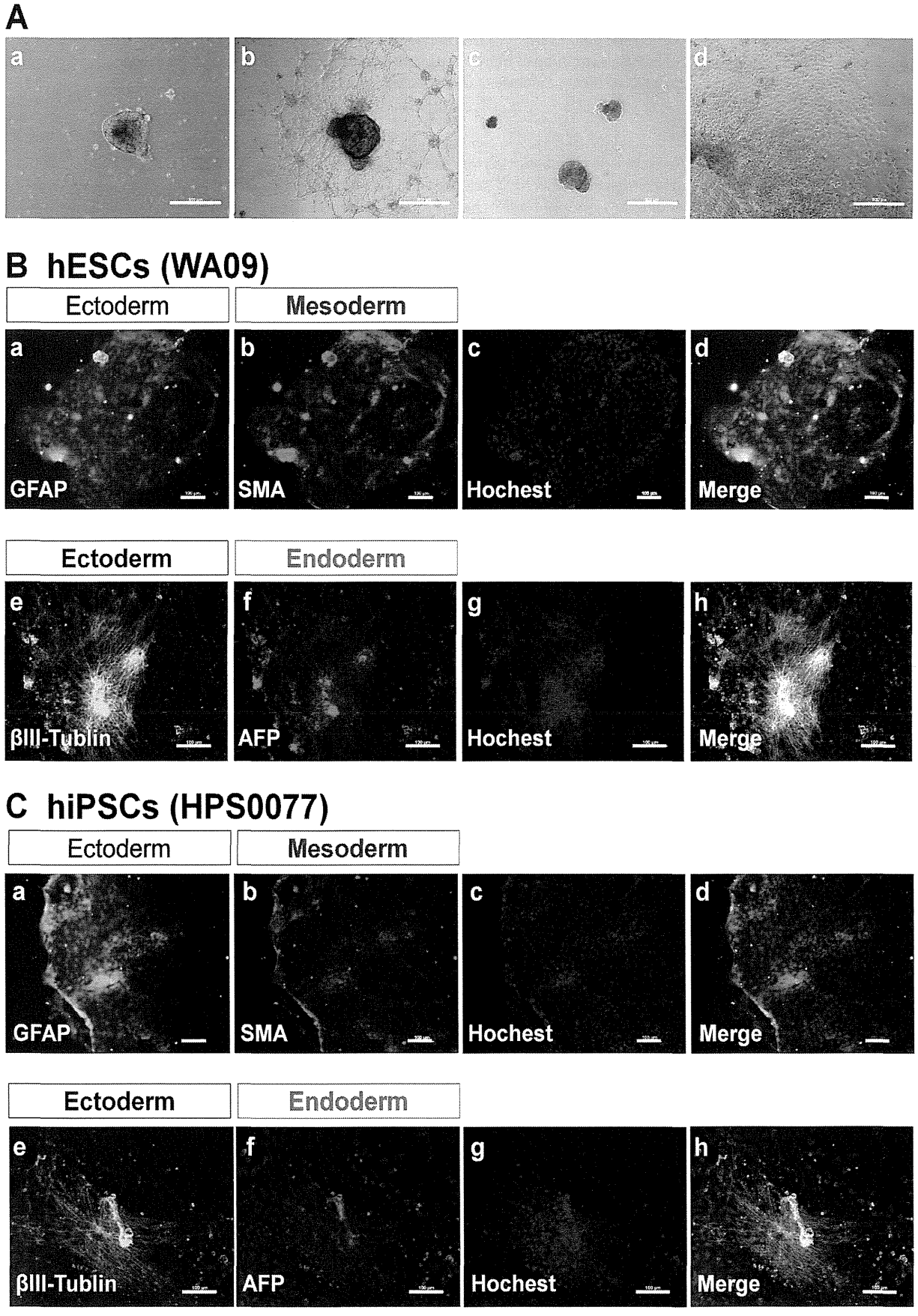

Figure 7. Characterization of the differentiation ability of hPSCs (hESCs and hiPSCs) *in vitro* after culture on PVA-oligoVN hydrogels for 20 passages. (**A**) Morphology of EBs differentiated from hESCs (WA09, **a,b**) and hiPSCs (HPS0077, **c,d**) after culture on PVA-24h-1000 dishes under xeno-free conditions for 20 passages. (**B**) Immunostaining of an ectoderm protein (**a**, GFAP; **e**, βIII-tubulin), mesoderm protein (**b**, SMA), and endoderm (**f**, AFP) protein on hESCs (WA09) after culture on PVA-24h-1000 dishes under xeno-free conditions for 20 passages. (**c**) Hoechest staining of hESCs used in (**a,b**). (**d**) Merged picture of (**a–c**). (**g**) Hoechest staining of hESCs used in (**e,f**). (h) Merged picture of (**e–g**). The bar indicates 100 μm. (**C**) Immunostaining of an